Cell

Microcephaly Gene Links Trithorax and REST/NRSF to Control Neural Stem Cell Proliferation and Differentiation

Yawei J. Yang,[1,3,4,5,7,8] Andrew E. Baltus,[1,7,16] Rebecca S. Mathew,[6,7] Elisabeth A. Murphy,[1,7,9] Gilad D. Evrony,[1,3,4,5,7] Dilenny M. Gonzalez,[1,7] Estee P. Wang,[1,3,7,10,17] Christine A. Marshall-Walker,[1,7,18] Brenda J. Barry,[1,7] Jernej Murn,[2,6] Antonis Tatarakis,[6,7] Muktar A. Mahajan,[11] Herbert H. Samuels,[11] Yang Shi,[2,6] Jeffrey A. Golden,[12] Muhammad Mahajnah,[13,15] Ruthie Shenhav,[14,15] and Christopher A. Walsh[1,3,4,7,*]

[1]Division of Genetics and Manton Center for Orphan Disease Research
[2]Division of Newborn Medicine
Boston Children's Hospital, Boston, MA 02115, USA
[3]Broad Institute of MIT and Harvard, Cambridge, MA 02142, USA
[4]Program in Biological and Biomedical Sciences
[5]Harvard MD-PhD MSTP Program
[6]Department of Cell Biology
Harvard Medical School, Boston, MA 02115, USA
[7]Howard Hughes Medical Institute, 4000 Jones Bridge Road, Chevy Chase, MD 20815, USA
[8]Harvard-MIT Division of Health Sciences and Technology, 77 Massachusetts Avenue, Cambridge, MA 02139, USA
[9]Department of Neuroscience, Northeastern University, Boston, MA 02115, USA
[10]Harvard School of Dental Medicine, Boston, MA 02115, USA
[11]Department of Pharmacology and Medicine, New York University School of Medicine, New York, NY 10016, USA
[12]Department of Pathology, Brigham and Women's Hospital, Boston, MA 02115, USA
[13]Child Development and Pediatric Neurology, Hillel Yaffe Medical Center, Hadera 38100, Israel, The Technion, Israel Institute of Technology, Haifa 32000, Israel
[14]Raphael Recanati Genetics Institute, Rabin Medical Center, Beilinson Campus, Petah Tikva 49100, Israel
[15]These authors contributed equally to this work
[16]Present address: Addgene, Cambridge, MA 02139, USA
[17]Present address: Department of Orthodontics, University of Michigan, Ann Arbor, MI 48109, USA
[18]Present address: Phillips Academy Andover, Andover, MA 01810, USA
*Correspondence: christopher.walsh@childrens.harvard.edu
http://dx.doi.org/10.1016/j.cell.2012.10.043

SUMMARY

Microcephaly is a neurodevelopmental disorder causing significantly reduced cerebral cortex size. Many known microcephaly gene products localize to centrosomes, regulating cell fate and proliferation. Here, we identify and characterize a nuclear zinc finger protein, *ZNF335/NIF-1*, as a causative gene for severe microcephaly, small somatic size, and neonatal death. *Znf335* null mice are embryonically lethal, and conditional knockout leads to severely reduced cortical size. RNA-interference and post-mortem human studies show that ZNF335 is essential for neural progenitor self-renewal, neurogenesis, and neuronal differentiation. ZNF335 is a component of a vertebrate-specific, trithorax H3K4-methylation complex, directly regulating REST/NRSF, a master regulator of neural gene expression and cell fate, as well as other essential neural-specific genes. Our results reveal ZNF335 as an essential link between H3K4 complexes and REST/NRSF and provide the first direct genetic evidence that this pathway regulates human neurogenesis and neuronal differentiation.

INTRODUCTION

Brain development requires carefully regulated yet continuously changing patterns of gene and protein expression. Cerebral cortical neurons are formed from progenitors that at the earliest stages divide mainly symmetrically to expand the progenitor population. At later stages, these apical progenitors divide increasingly in an asymmetrical fashion to produce one progenitor cell and a second more differentiated cell—either a neuron or a transit-amplifying progenitor cell that resides in the subventricular zone (Lui et al., 2011). Eventually, symmetrical divisions of progenitors are increasingly replaced by neurogenic cell divisions that produce the neurons of the cerebral cortex in an inside-first, outside-last sequence (Fietz and Huttner, 2011). Although much is known about the cellular patterns of neurogenesis, the molecular controls of this process remain relatively poorly understood.

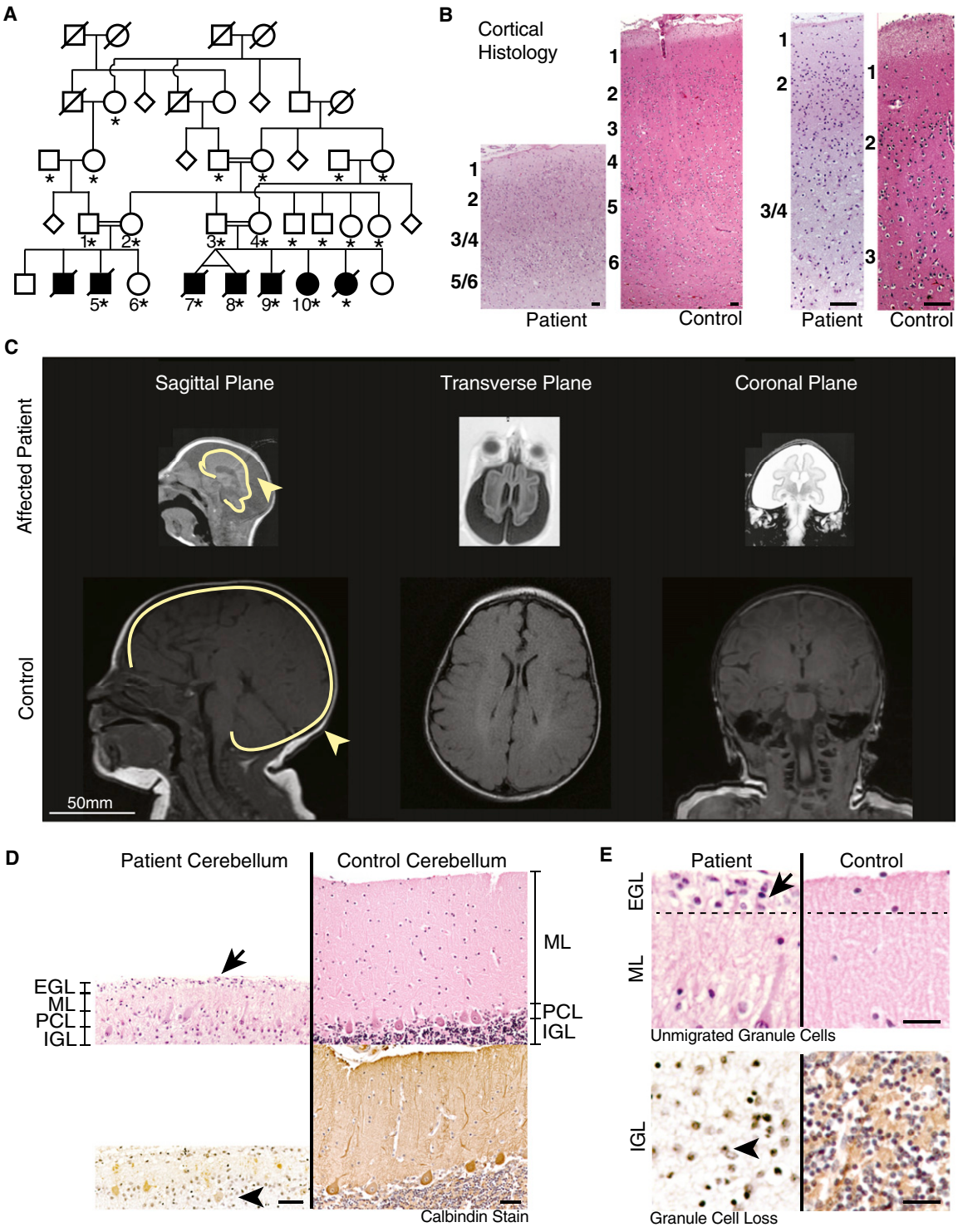

Figure 1. A New Syndrome of Severe Microcephaly and Neuronal Degeneration

(A) Pedigree of family with severe microcephaly. (Double lines) Consanguineous marriages; (black shading) known affected; (diagonal line) deceased at time of publication; (asterisk) sequence analysis was completed on the individual.

(B) Cortical histology of patient versus age-matched controls at 10× (left) and 40× (right) magnification. Patients show decreased cortical thickness and abnormal cortical layers. Scale bar, 300 μm.

(C) MRI of patient versus age-matched control shows decreased brain size, including cerebellum and brain stem, increased extraaxial space, and enlarged ventricles. Whole brains are outlined in yellow, showing separation of brain from skull.

Naturally occurring mutations of human cerebral cortical development have provided surprising genetic insights into the process of neurogenesis in vertebrates. Genetic causes of microcephaly implicate components of the mitotic spindle and proteins involved in DNA repair (Mahmood et al., 2011; Mochida, 2009; Thornton and Woods, 2009). However, human microcephaly genes have so far generally not highlighted the transcriptional pathways that animal studies implicate as essential to cerebral cortical neurogenesis (Molyneaux et al., 2007).

A key aspect of the regulation of gene expression during neurogenesis occurs at the level of chromatin structure. Acetylation, methylation, and phosphorylation of histone proteins affect the access of transcriptional proteins to DNA wrapped around nucleosomes (Bannister and Kouzarides, 2011), contributing to the complex control of gene expression. The trithorax (TrxG) and polycomb (PcG) chromatin-remodeling complexes work in opposition to activate or silence gene expression, respectively (Ng and Gurdon, 2008). Recent studies shed light on the importance of chromatin regulatory complexes in brain development and developmental disease, although focus is placed mostly on PcG complex proteins and adult neurogenesis (Lessard and Crabtree, 2010; Ma et al., 2010). TrxG regulates developmental expression of many genes that are important for patterning, cell proliferation, and stem cell identity by maintaining genes in an active state (Fisher and Fisher, 2011). The TrxG complex activates gene expression through the methylation of lysine 4 on histone H3 (H3K4) (Papp and Müller, 2006), a marker of actively transcribed genes or genes poised for transcription (Bernstein et al., 2005). SET1 methyltransferases (MLL1, MLL2, and SET1A/B) are the major enzymes carrying out H3K4 methylation, functioning in a multiprotein complex with Ash2L, WDR5, and RbBP5 (Schuettengruber et al., 2011). Although TrxG has been implicated in *Drosophila* development (Paro et al., 1998) and members of the complex have been implicated in vertebrate development and embryonic stem cells (Ang et al., 2011), the role of TrxG has not been well studied in neural stem cells or in human brain development (Schuettengruber et al., 2011).

Another critical epigenetic regulator of neurogenesis is the repressor element 1 (RE1)-silencing transcription factor (REST)/neuron-restrictive silencer factor (NRSF) (Chong et al., 1995; Schoenherr and Anderson, 1995). REST/NRSF acts as a transcriptional repressor through the recruitment of histone deacetylases (HDACs), which place chromatin in a condensed state via the removal of acetyl residues (Ballas et al., 2005). REST/NRSF is expressed in neural stem cells and is essential for maintaining progenitor cell fate by inhibiting neuronal specific genes (Sun et al., 2005). REST/NRSF has also been suggested to play roles in embryonic stem cells as well as mature cell types (Ballas et al., 2005; Johnson et al., 2008); however, the upstream regulation of REST/NRSF, as well as the interaction of REST/NRSF and TrxG, two central epigenetic regulators of neurogenesis, is unknown.

In this study, we identify a new regulator of vertebrate neurogenesis, *ZNF335*, in a family that presents with one of the most severe cases of microcephaly documented. ZNF335 was previously cloned and identified as a coregulator (NRC-interacting factor 1 [Nif1]) of nuclear hormone signaling (Garapaty et al., 2009) and as part of a complex containing components known to be involved in histone H3 methylation, but its functions have never been studied in vivo. We show that *ZNF335* is essential for normal brain development in human and mouse and that ZNF335 interacts with a H3K4 chromatin methyltransferase complex. ChIP-PCR, ChIP-seq, RNA-seq, and microarray studies reveal that ZNF335 is essential for methylation and expression of brain-specific genes including the master progenitor regulator REST/NRSF. Knockdown of ZNF335 disrupts progenitor cell proliferation, cell fate, and neuronal differentiation. Brain-specific knockout leads to severely reduced to absent forebrain structure. Together, these data define an essential control system for REST/NRSF expression and implicate a new microcephaly gene that coordinates global transcriptional regulation in brain development to affect cell fate.

RESULTS

A New Syndrome of Profound Microcephaly, Neuronal Degeneration, and Neonatal Death

A large consanguineous Arab Israeli pedigree presented with seven individuals (two of them identical twins) affected with one of the most severe cases of microcephaly (MCPH) seen to date (head circumference 9 standard deviations below mean) and death by 1 year of age in all but one case (Figures 1A–1C). MRI at 3 months of age revealed extreme microcephaly with a severely simplified gyral pattern (Figure 1C). The cerebral cortex was even more notably smaller than the skull, with subarachnoid fluid separating the two, an indication of secondary shrinkage of the brain usually reflecting degeneration (Barkovich et al., 2007). Histopathology of Patient 5 at 7 months of age revealed a thinned cerebral cortex and neuronal disorganization, with only about 20% of the cortex showing the normal six cortical layers (Figure 1B). The few neurons that were present demonstrated little apparent polarity or dendritic maturation. Layer I, a normally cell-sparse layer containing many neuronal processes, was severely reduced in thickness, potentially reflecting defects in process outgrowth and/or defects of layer I Cajal-Retzius cells. Layers II–VI, normally neuron rich, showed sparse neurons of abnormally small size, suggesting incomplete neuronal differentiation. Well-differentiated pyramidal neurons, normally the most abundant neuron in the cortex, were also almost completely unidentifiable because of either aberrant differentiation or severely reduced numbers (Figure 1B).

(D) Cerebellar histology. Calbindin-stained sections of patients versus age-matched controls. Patients have persistent external granule cell layer (EGL), decreased molecular layer (ML), abnormal Purkinje cell layer (PCL), and decreased internal granule cell layer (IGL). Scale bar, 100 μm.

(E) Patients have unmigrated EGL cells (top, arrow) above a thinner molecular layer. Patients have severely reduced granule cell density compared to control (bottom, arrowhead). Scale bar, 50 μm.

See also Extended Experimental Procedures.

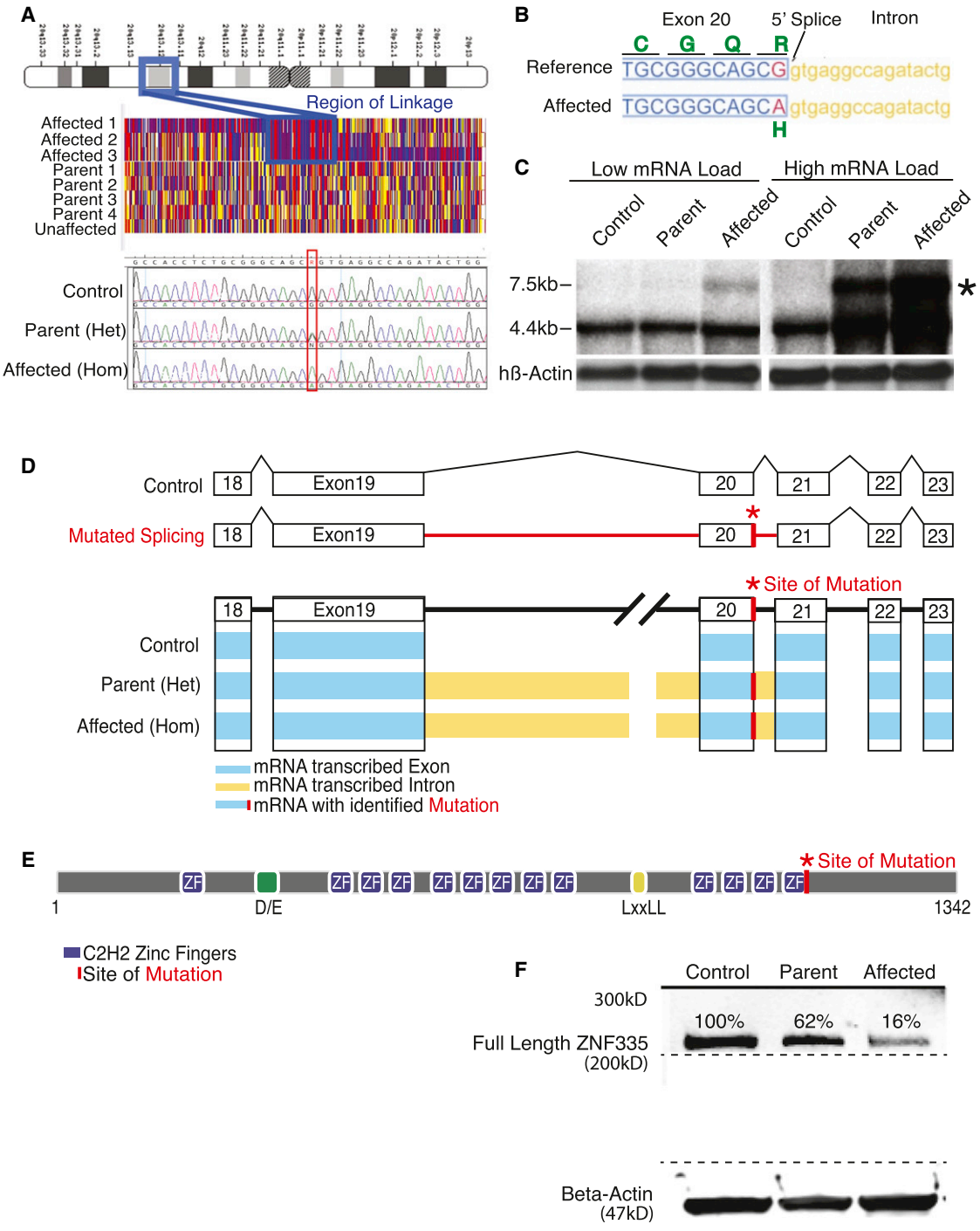

Figure 2. Severe Microcephaly Reflects a Splicing/Missense Mutation *ZNF335*

(A) Patients show linkage at chromosome 20q13.12. Sequencing shows a c.3332g>a mutation in gene *ZNF335*. (Top) Schematic of chromosome 20. (Middle) Single-nucleotide polymorphism genotyping. Each column represents a SNP, and the red and blue indicate homozygosity, whereas yellow shows heterozygosity. A large region (boxed) shows mainly red and blue SNPs in affected patients with heterozygosity in parents. (Bottom) Representative sequencing data.

(B) Mutation is at a 5′ splice site of *ZNF335* and leads to p.R1111>H missense mutation.

(C) Northern blot shows production of a new larger transcript (*) in heterozygous parents and homozygous patients. Amino acid sequence (green); exon sequence (blue); intron sequence (yellow); mutation (red).

(D) Schematic of exons and intronic splicing for a control, and the predicted problems with intronic splicing in a patient with a c.3332g>a mutation. Schematic of RNA-seq data shows detection of reads within exons (blue) and within introns (yellow) upstream and downstream of the mutation-containing exon. Incomplete splicing is present in heterozygous parents (Het) and homozygous patients (Hom), but not in control cells. RNA-seq data also detected the base change mutation (*).

The cerebellum showed severely reduced external as well as internal granule cell layers (EGL, IGL), which normally contain granule cell precursors and granule cells at this age (Figure 1D), suggesting widespread loss. There were few Purkinje cells and increased numbers of eosinophilic gemistocytic astrocytes in the Purkinje cell layer (PCL), consistent with a degenerative process. Calbindin immunoreactivity highlighted the severely reduced number and abnormal localization and orientation of the rare remaining Purkinje cells (Figure 1D). A few mature granule cells persisted in the EGL (Figure 1E, top), suggesting defective migration into the IGL. There is also a strikingly cell-sparse IGL, normally the location of countless mature granule cells (Figure 1E, bottom), suggesting profound defects in generation and/or survival. These postmortem histological studies suggest that the responsible gene has essential roles in normal neurogenesis, neuronal migration, and neuronal polarity, as well as neuronal survival. The small birth weight and length and other somatic features indicate that somatic size was affected, as well as brain size (Extended Experimental Procedures available online).

A Splice Donor/Missense Mutation of *ZNF335* Causes Severe Microcephaly

The genetic mutation was identified by linkage mapping and gene sequencing and was confirmed and further characterized using mRNA-transcriptome sequencing (RNA-seq). Mapping using single-nucleotide polymorphism (SNP) arrays, followed by fine mapping, identified a single ~2 Mb interval that was homozygous and identical by descent in all affected pedigree members (Figure 2A) and in none of the unaffected individuals (multipoint logarithm of odds [LOD] = 4.54). Sequence analysis of the 40 genes in the minimal linked region showed only one homozygous nonsynonymous change not already identified in dbSNP: a G-to-A transition at position 3332 of the coding sequence of the *ZNF335* gene. All affected individuals were homozygous for this mutation, all parents were heterozygous, and an unaffected sibling was wild-type, consistent with an autosomal recessive mode of inheritance (Figures 1A and 2A). This change was absent from 100 Middle Eastern control patients, 200 sequenced-unaffected Arabic control exomes, and 2,500 European control exomes (NHLBI GO Exome Sequencing Project), confirming that it is not a rare benign change. This c.3332g>a mutation results in a predicted change of Arg R (CGC) at amino acid position 1111 of the ZNF335 protein to His H (CAC) (Figure 2B). Moreover, the c.3332g>a transition is located at the final position of the splice donor site of exon 20, and a G at this position is highly conserved in mammalian splice donor sites (Cartegni et al., 2002).

Northern analysis and RNA-seq from lymphocyte cell lines derived from an affected patient and a heterozygous parent confirmed that the c.3332 g > a mutation disrupted normal splicing. Whereas a cell line from an unrelated individual showed a normal 5 Kb transcript (Figure 2C), both affected patient and heterozygous carriers showed a larger transcript absent in the control, suggesting that the c.3332g>a mutation produces a larger transcript with intron retention. Presence of normally sized transcripts in homozygous mutant lymphocytes suggests that some normally spliced RNA (albeit encoding a p.R1111H mutation) is still formed. RNA-seq of cytoplasmic RNA verified the *ZNF335* mutation and also revealed abnormal *ZNF335* transcripts with inclusion of both the introns (introns 19, 20) flanking the mutation-containing exon (Figures 2D and S1A) at significantly higher levels than in control cells (p value of 1.57×10^{-31}).

Western analysis of homozygous patient cells showed severely reduced ZNF335 protein levels at the previously reported size of ~190 kD (Figure 2F). The inclusion of introns 19 and 20 leads to a premature stop codon that could cause transcript degradation (Isken and Maquat, 2007). Yet, a small amount (≈16% of control) of full-length, R1111H-mutated protein is still formed, suggesting that some transcript splices normally (Figure 2F), although this mutated protein appears to be less stable (data not shown). No larger protein or degraded protein products were detected in the heterozygous parent or affected patient. Evolutionary analysis of available *ZNF335* orthologs indicates that R1111 falls in the 13th zinc finger domain (Figure 2E), which is absolutely conserved in all known *ZNF335* sequences (Figure S1B). Interestingly, no clear *ZNF335* ortholog can be identified outside of vertebrates. These results are all consistent with the hypothesis that the identified mutation in *ZNF335* is the causative mutation in this family. The ortholog in *Mus musculus* is the *Zfp335* gene, but for simplicity, we will use *Znf335* throughout this manuscript.

ZNF335 Is Essential for Early Embryonic Mouse Development

In order to confirm that ZNF335 is essential in early brain development, we examined mice with engineered null *Znf335* mutations and observed that homozygous loss of ZNF335 leads to early embryonic lethality as early as embryonic day 7.5 (E7.5) (Figures 3A and S2A–S2C). This essential requirement of ZNF335 suggests that the human R1111H mutation could be hypomorphic, as it results in some stable protein, albeit carrying a missense mutation. Examination of 100 individuals with varying degrees of microcephaly—though none as severe—showed no other patients with *ZNF335* mutations, suggesting that null *ZNF335* mutations in humans may also be lethal. Our data suggest that *ZNF335* is essential for normal human brain development and mouse development and prompted us to examine its function.

The pattern and timing of ZNF335 expression are consistent with roles in neurogenesis and potentially other processes as well. Northern analysis of adult (Figure S2A) and embryonic (Figure S2B) human tissues revealed widespread expression of

(E) Predicted structure of ZNF335. Mutation lies in the last zinc finger motif.

(F) Western blot of patient lymphoblast cell lines shows that heterozygous parents and homozygous patients produce a reduced amount of full-length ZNF335 protein and shows no evidence of larger or degraded protein products.

See also Figure S1.

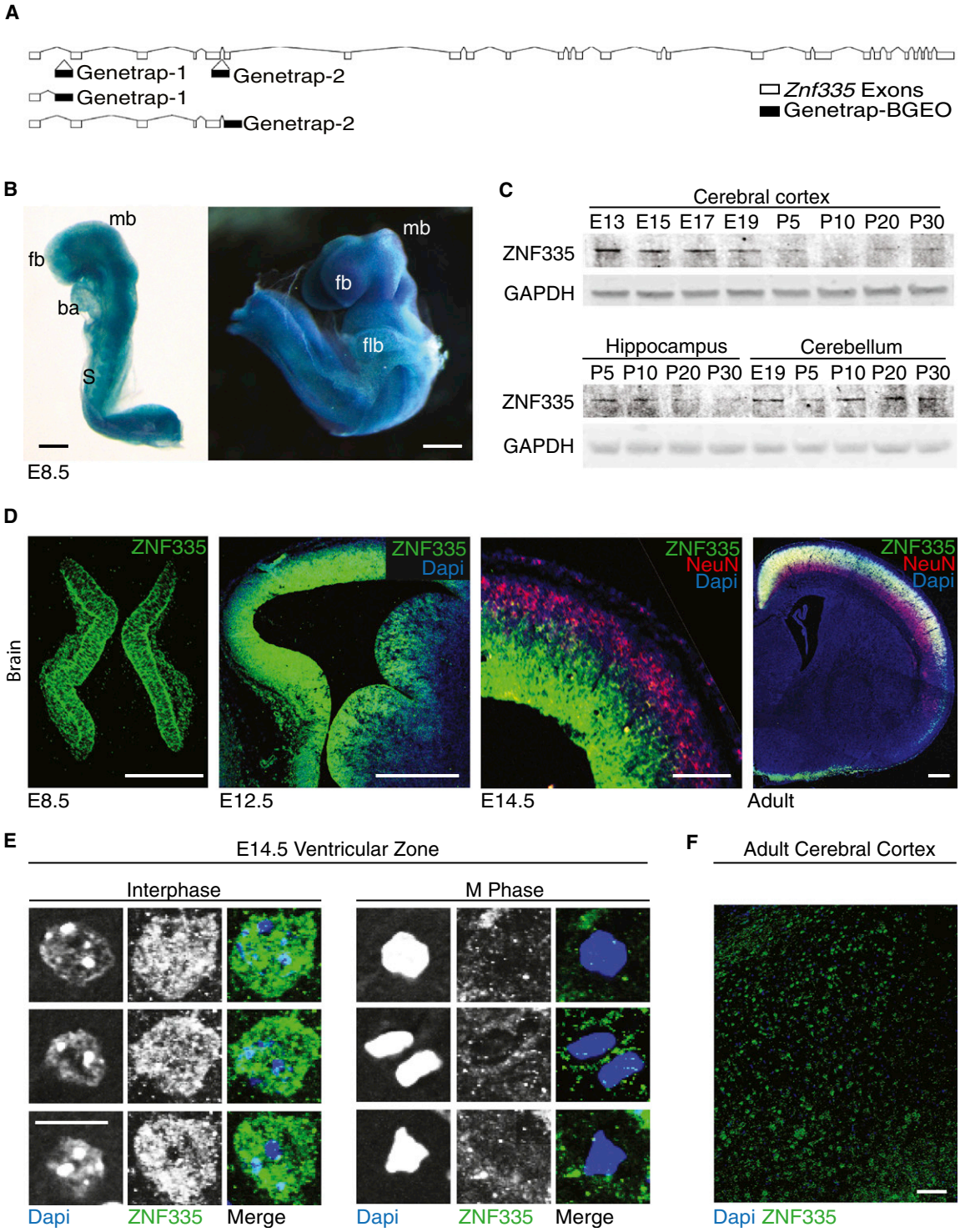

Figure 3. ZNF335 Is Essential for Mouse Development and Is Expressed in Nuclei of Progenitor Cells

(A) Location of genetrap insertion of two genetrap mouse lines leading to early truncation of protein to mimic a null allele.

(B) ZNF335 is expressed at E8.5 in developing forebrain (fb), midbrain (mb), somites (S), Branchial arch (ba), and Forelimb bud (flb). Scale bar, 300 μm.

(C) Western blot analysis of ZNF335 protein expression throughout brain development. In the cortex, expression is highest at E13 before tapering off, and expression returns slightly postnatally. ZNF335 is also expressed during the peak of hippocampal and cerebellar development.

(D) Immunohistochemistry shows ZNF335 expression in progenitor cells at E8.5 and in the ventricular zone and subventricular zone of the developing cortex, but not in NeuN+ neurons at E14.5. Protein is also expressed throughout cortical plate later in development. Scale bars, 50, 50, 50, and 400 μm.

ZNF335, including during embryonic brain development. Western analyses of mouse brain tissue show that ZNF335 expression peaks at the height of cortical neurogenesis from E13–E15 (Figure 3C). To localize the expression of ZNF335 in specific cell populations, heterozygous genetrap mice containing a β-galactosidase fusion reporter gene were stained histochemically. ZNF335-lacZ was expressed in the developing forebrain and midbrain of E8.5 embryos (Figures 3B and 3D). Immunofluorescence analysis using antisera raised against ZNF335 confirmed expression in the ventricular zone (VZ) and subventricular zone (SVZ), as well as at lower levels in the developing cortical plate, but showed almost undetectable expression in NeuN-labeled neurons of the cortical plate at E14.5 (Figure 3D). At P5–P30, ZNF335 expression returns at low levels in the adult cerebral cortex, hippocampus, and cerebellum, possibly linked with neuronal maturation (Figures 3C, 3D, 3F, S2D, and data not shown). Higher magnification showed ZNF335 immunoreactivity in nuclei of progenitor cells, where it colocalizes with DAPI-stained DNA (Figure 3E), but it was largely or completely absent from heterochromatic foci. This expression pattern is consistent with roles of ZNF335 in the progenitor cells prenatally and with possible roles in gene expression.

ZNF335 Regulates Neural Progenitor Self-Renewal and Neurogenesis

The expression of ZNF335 in progenitor cells along with the reduced brain size of patients hint at a role in regulating proliferation. In addition, lymphoblast cell lines from patients show decreased growth (Figure 4A), and the p.R1111H mutation leads to decreased ZNF335 binding with Ki-67, a component of a chromatin complex expressed in virtually all proliferating cells and required for growth and survival (Figure S3A) (Garapaty et al., 2009; Zheng et al., 2006). To assess roles of ZNF335 in progenitor proliferation directly, we selectively removed ZNF335 from cerebral cortical progenitor cells by electroporating GFP-expressing plasmids that express either an shRNA against *Znf335* (shRNA-ZNF335, Figure S3B–S3C) or an shRNA containing silent mutations, making it unable to target *Znf335* (UT-Control). Electroporation was performed into cortical progenitor cells at E9.5 and E12.5. Targeted cells were selected upon dissociation using fluorescent-activated cell sorting (FACS) 24 hr postelectroporation, and the formation of proliferating reaggregate spheres was used to assess progenitor cell proliferation. Knockdown of ZNF335 in both E9.5 and E12.5 progenitors led to a decrease in reaggregate sphere formation (Figure 4B), confirming the role of ZNF335 in progenitor cell proliferation and self-renewal.

In utero electroporation into developing cortices allowed targeting of cortical progenitor cells along the ventricular zone and follow-up studies in the native three-dimensional (3D) architecture of the brain. At 48 hr postelectroporation, fewer ZNF335-depleted cells were observed in the VZ (Figures 4C and 4E), and this phenotype could be rescued by wild-type ZNF335 (WT-ZNF335), but not by mutated ZNF335 (MUT-ZNF335) (Figures 4C, 4E, and S3D). Bromodeoxyuridine (BrdU) pulse-labeling experiments showed that this decrease reflected fewer progenitor cells undergoing DNA synthesis even 24 hr postknockdown (Figure 4F). A BrdU/Ki67 colabeling experiment was performed to mark progenitor cells that either remained in the cell cycle (P fraction) or exited the cell cycle (Q fraction). By 48 hr postknockdown, a greater proportion of targeted progenitor cells exited the cell cycle as compared to UT-Control or wild-type (WT) unelectroporated controls (Figures 4D and 4G). Taken together, these data show that ZNF335 is essential for progenitor self-renewal by maintaining progenitors in the cell cycle and preventing premature cell-cycle exit.

We confirmed the premature cell-cycle exit of ZNF335-depleted cells by allowing electroporated mice to develop until adulthood. A higher proportion of ZNF335-depleted neurons occupied deeper layers of the cortex (Figure 4H, 4I), consistent with early cell-cycle exit, and fewer occupied more superficial layers, the location of later born neurons. ZNF335-depleted neurons also exhibited abnormal cell fates. Whereas most control neurons were Cux1 positive and FoxP1 negative (markers of layers II–IV and III–V, respectively), knockdown neurons instead took on the identity of lower-layer, earlier born neurons (Cux1 negative, FoxP1 positive) (Figures 5A and 5C). These data indicate that ZNF335 deficiency leads to premature neuronal fate determination, which causes a depletion of dividing cells and is consistent with our patient phenotype of reduced cortical size and abnormal cortical layering.

ZNF335 Also Regulates Neuronal Morphogenesis and Dendrite Outgrowth

Further analysis of ZNF335-depleted neurons demonstrates abnormal neuronal morphology reminiscent of the patient histology (Figures 1B and 1D). Knockdown cells at P0 showed abnormal cell orientation and radial glia (Figure 5Ba and 5Bb). By P6 and P8, knockdown neurons showed smaller cell bodies and lacked normal vertical apical dendritic process (Figure 5Bc–5Bf). By P16, the dendritic outgrowth of knockdown cells was disorganized and abnormally oriented (Figures 5Bg and 5Bh), and only 25% of cells showed dendrites orientated perpendicular to the pial surface, versus 95% in controls (Figure 5D). By adulthood, knockdown neurons showed disorganized branching, abnormal orientation, and signs of breakdown in dendrites (Figure 5Bi–5Bn). WT-ZNF335, but not MUT-ZNF335, rescued the orientation phenotype, confirming the specificity of this phenotype and that the p.H1111R mutation is deficient but likely hypomorphic (Figure 5D). These phenotypes are reminiscent of the sparse neurons with reduced dendrites and abnormal orientation seen in patient histology studies. Microarray analysis of neurons with decreased ZNF335 expression showed decreased expression of genes

(E) ZNF335 localizes to the nucleus and colocalizes with euchromatin of progenitor cells in the ventricular zone of developing mouse brain, whereas ZNF335 is excluded from heterochromatic foci. This colocalization disappears in cells in the M phase of the cell cycle. Scale bar, 10 μm.
(F) Sparse expression of ZNF335 in adult cerebral cortex. Scale bar, 100 μm.
See also Figure S2.

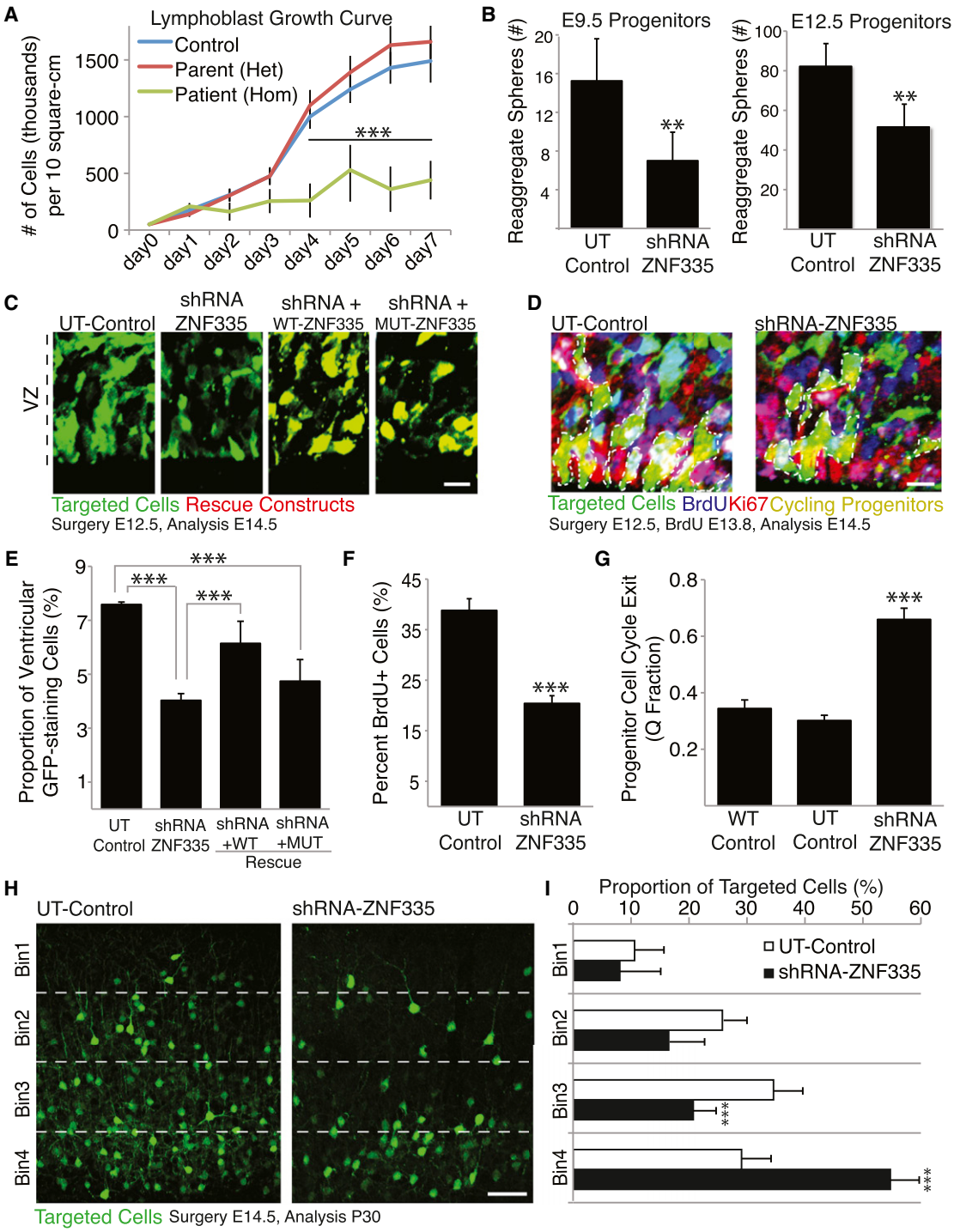

Figure 4. ZNF335 Is Essential for Progenitor Cell Proliferation and Cell-Cycle Maintenance

(A) Growth curves of lymphoblast cell lines derived from heterozygous parent (Het), homozygous patient (Hom), and control shows decreased growth rate in cells from patient with low levels of mutated ZNF335.

(B) Knockdown of ZNF335 leads to decreased formation of progenitor cell reaggregates in E9.5 and E12.5 progenitor cell cultures showing decreased proliferation upon knockdown of ZNF335. E9.5: UT-Control, 15.25 ± 4.3; ShRNA-ZNF335, 7.1 ± 2.9, t test, $p = 0.0032$, $n = 6$; E12.5 UT-Control, 82.2 ± 11.5; ShRNA-ZNF335, 51.6 ± 11.6. T test, $p = 0.001$; $n = 6$ rounds of FACS sorting, mean ± SD. Each sort is from pooled embryos from three different dams with roughly half of their embryos electroporated with either shRNA-ZNF335 or UT-control constructs.

(C) shRNA-ZNF335 knockdown leads to fewer cells present within the ventricular zone when compared to UT-Control. WT-ZNF335 rescues the number of progenitors, but MUT-ZNF335 does not. Scale bar, 10 μm.

that are important for brain development, such as neuron-specific transcription factors, dendritic branching and pruning genes, cell-cycle and specific signaling factors, and neuronal-specific microtubule-binding partners (Figure S4), all of which could contribute to the neuronal and patient phenotypes.

ZNF335 Interacts with a Chromatin-Remodeling Complex

In order to elucidate how loss of ZNF335 could have such broad roles, we identified candidate-interacting proteins by immunoprecipitating (IP) FLAG-tagged ZNF335 in stable HeLaS3 cell lines as well as from endogenous E14.5 developing mouse brain lysates. Experiments utilizing IP followed by mass spectrometry (MS) and western verification revealed that ZNF335 pulls down members of a human H3K4 methyltransferase complex such as MLL, SETD1A, CFP1, ASH2, RbBP5, and WDR5 and that the complex components have histone H3 methyltransferase activity (Figure 6A and Table S1) (Garapaty et al., 2009; Schuettengruber et al., 2011). Together, these proteins form a complex analogous to that of the TrxG complex in *Drosophila* or the complex COMPASS (complex proteins associated with Set1) in *Saccharomyces cerevisiae*—both required for specific activation of gene expression (Schuettengruber et al., 2011). Knockdown of members of this methyltransferase complex cause stunted embryonic development and death, whereas WDR5 expression activates self-renewal genes in embryonic stem cells (Ang et al., 2011). The interaction of ZNF335 with a H3K4 methyltransferase complex presents an avenue for the regulation of many genes, consistent with the widespread effects in the brain and other tissues upon ZNF335 loss.

ZNF335 Regulates Histone Methylation and Expression of Specific Genes

Chromatin IP followed by deep sequencing (ChIP-seq) identified ZNF335-bound promoters representing possible ZNF335-regulated genes. ChIP-seq was performed on developing mouse E14.5 lateral telencephalon with two separate antisera and two biological replicates. ZNF335 peaks overlapped with promoter regions (Figures 6B, 6C, and S5) of a variety of genes, for example, genes that play roles in cell proliferation, somatic development, cell death, neuronal maturation, and signaling pathways, among others (Figure S5 and Table S2). Because ZNF335 interacts with a methyltransferase complex, we looked at the methylation patterns of these ZNF335-bound promoters (Shen et al., 2012), and the peaks of ZNF335 binding overlapped with the H3K4 trimethylation (H3K4me3) peaks (Figure S5A). Similarly, in patients with decreased ZNF335, H3K4me3 marks at the promoters of ZNF335-bound genes were also decreased, whereas control H3K27me3 marks were unchanged (Figure S5B). Finally, because H3K4me3 is linked with gene expression, RNA-seq data from the parents and patients with low H3K4me3 marks also showed decreased expression of these ZNF335 target genes (Figure S5C and Table S2). Together, these data hint at a role of ZNF335 in a methyltransferase complex that is important for the H3K4 trimethylation and ultimately the expression levels of a large variety of genes. GeneGo analysis performed on the genes identified through ChIP-seq, microarrays, and RNA-seq data from patients showed that the genes affected by ZNF335 were involved in a variety of pathways that are important for both somatic development and brain development (Tables S3–S6).

ZNF335 Is Upstream of REST/NRSF

Interestingly, we observed ZNF335 bound to the promoter region of the known progenitor cell master regulator *REST/NRSF* (Figure 6B). A direct relationship between ZNF335 and expression of *REST/NRSF* is suggested by decreased TrxG complex binding and decreased H3K4me3 marks at the *REST/NRSF* promoter (Figures 6D and 6E), as well as by decreased mRNA levels of *REST/NRSF* in *ZNF335* mutant patients (Figure 6E). Decreased *REST/NRSF* expression was seen upon ZNF335 knockdown of HeLa and Hek293 cells (Figure 6G), supporting a close and potentially direct relationship. Conversely, expression of a dominant-negative REST (DN-REST), which contains the DNA-binding domain only (Chong et al., 1995; Schoenherr and Anderson, 1995), as well as overexpression of REST/NRSF, did not significantly alter *ZNF335* expression (Figure 6H). Rescue experiments also showed that premature cell-cycle exit and premature migrating neurons in the absence of ZNF335 could be rescued by REST, but not by DN-REST, which caused a phenotype similar to ZNF335 deficiency (Figure 6J). These data, along with the promoter binding of REST/NRSF by ZNF335, suggest direct regulation of REST/NRSF expression by ZNF335 (Figure 6I) and provide an avenue for

(D) shRNA-ZNF335 knockdown leads to fewer cycling progenitors in the ventricular zone as compared to the UT-Control. Scale bar, 10 μm.

(E) Quantification of (C). Knockdown of ZNF335 leads to fewer percentage of targeted cells present within 250 μm^2 of the ventricular zone as compared to UT-control. WT-ZNF335 rescues the amount of GFP-staining cells in the VZ, whereas MUT-ZNF335 does not. UT-control: 7.59 ± 0.09; ShRNA-ZNF335: 4.0 ± 0.25; shRNA+WT-ZNF335: 6.27 ± 0.70; shRNA+MUT-ZNF335: 4.74 ± 0.80, mean ±SD, t test, p = 0.0001; n = 12 means from different electroporated litters.

(F) Knockdown of ZNF335 leads to fewer cells that are BrdU positive 48 hr postknockdown within 50 μm^2 of the ventricular zone as compared to UT-control. UT-Control: 38.8 ± 2.9; shRNA-ZNF335: 20.4 ± 1.7, mean ±SD, t test, p = 0.0001; n = 12 electroporated brains that were analyzed using serial sections.

(G) Knockdown of ZNF335 leads to increased cell-cycle exit (decreased BrdU+/Ki67+ cells out of total BrdU+ cells) as compared to UT-Control. WT-Control: 0.34 ± 0.03; UT-Control: 0.30 ± 0.02; ShRNA-ZNF335: 0.66 ± 0.04, mean ±SD, ANOVA, p < 0.0001; n = 12 electroporated brains that were analyzed using serial sections.

(H) Knockdown of ZNF335 as compared to control leads to more targeted cells in the lower layers of the mouse cortex and fewer targeted cells in upper layers of the mouse cortex, indicating more premature neurogenesis upon knockdown of ZNF335. Earlier born neurons reside in deeper layers versus later born neurons that reside in the upper layers. Scale bar, 50 μm.

(I) Cortex was divided into equal-sized bins and was counted for proportion of targeted cells present in that bin. UT-Control: Bin1: 10.6 ± 4.9; Bin2: 25.8 ± 3.7; Bin3: 34.6 ± 5.2; Bin 4: 29.1 ± 4.8; *shRNA-ZNF335*: Bin1: 8.1 ± 7.1; Bin2: 16.5 ± 6.1; Bin3: 20.7 ± 3.6; Bin4: 54.7 ± 5.1. mean ±SD, t test; Bin3: p = 0.0003, Bin4: p = 0.0001; n = 12 electroporated brains. Only matching sections between conditions were compared.

See also Figure S3.

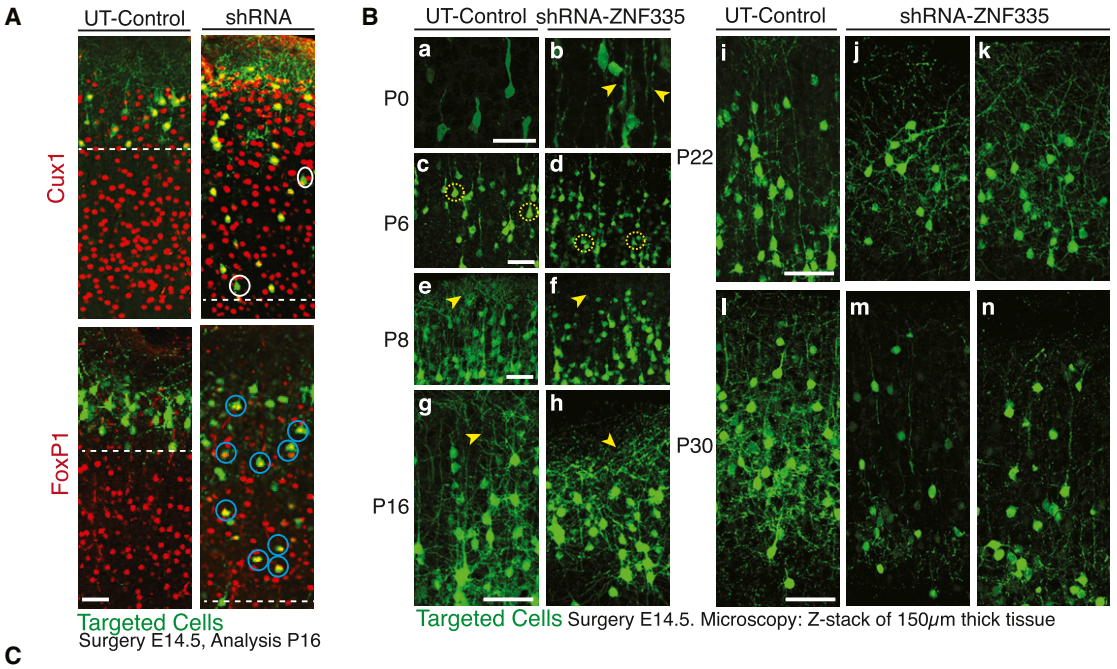

C

Cell Counts Cux1 FoxP1

	Cux1+	Cux1-
UT-Control	95.5 +/- 4.5	4.5 +/- 4.5
shRNA	88.2 +/- 3.6	12.8 +/- 3.6

	FoxP1+	FoxP1-
UT-Control	5.4 +/- 3.9	94.6 +/- 3.9
shRNA	34.3 +/- 8.6	65.7 +/- 8.6

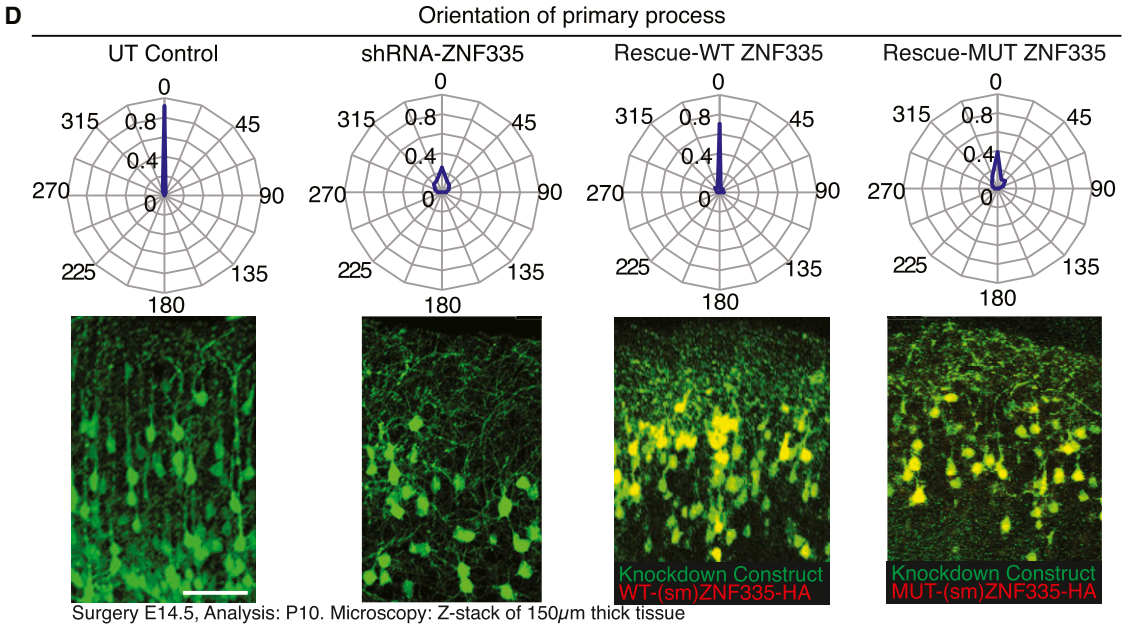

Figure 5. ZNF335 Deficiency Leads to Decreased Cell Size and Abnormal Dendritic Shape and Orientation

(A) Knockdown of ZNF335 leads to reduction of cells in the cortical plate and production of Cux1-negative (white circles) and FoxP1-positive (blue circles) cells showing a change in cell fate. Dashed line represents end of zone containing GFP-positive cells. Scale bar, 50 μm.

(B) Knockdown and control cells were targeted at E14.5 and analyzed at P0 (a and b), P6 (c and d) to show abnormal radial glia (P0, arrowhead) and abnormal cell body shape and size (P6, dashed circle). There is abnormal dendritic arborization (arrowhead) and orientation in knockdown cells at P8 (e and f) and P16 (g and h) and signs of breakdown in dendrites at P22 (i, j, and k) and P30 (l, m, and n). Scale bar, 50 μm.

(C) Analysis of (A). Knockdown showed production of more Cux1-negative cells as compared to control and production of more FoxP1-positive cells as compared to control.

abnormal neurogenesis secondary to abnormal REST/NRSF regulation.

Roles of ZNF335 in Neuronal Production and Differentiation

Further analysis of ZNF335 knockdown neurons showed stereotypical neuronal morphology (small cell bodies, dendrites, axons) but with a surprising loss of immunoreactivity for D11Bwg0517e/Fox3, or neuronal nuclei (NeuN), a ubiquitous marker of all differentiated neurons (Dredge and Jensen, 2011) (Figures 7A, 7B, and S6A), suggesting an apparent state of incomplete neuronal differentiation. This failure to express mature neuronal markers could reflect the abnormal premature neurogenesis caused by early progenitor cell-cycle exit (Figure 4D) or, perhaps more likely, could reflect direct requirements for ZNF335 in controlling gene expression in postmitotic neurons or in neuronal maturation and activity. The altered morphology (Figure 5B) and the arrested development (Figure 7A) exhibited by ZNF335 knockdown neurons are reminiscent of the altered neuronal phenotype, cortical layers, and cortical size seen in patients (Figures 1B and 1C).

Similar to ZNF335-depleted cortical neurons, ZNF335 knockdown in cerebellar granule cells produced abnormal cell migration, morphology, and differentiation. ZNF335-deficient cerebellar granule cells showed migration arrest with decreased migration into the IGL (Figures S6B and S6C) recapitulating the human phenotype (Figures 1D and 1E). Microarray (Figure S4) and immunohistochemistry (Figures 7C and 7D) of ZNF335-deificient cells showed decreased Mef2C expression, suggesting an arrest of normal transcriptional patterns. Our findings that knockdown of ZNF335 leads to increased cell death (Figure S6D) might suggest that this effect is mediated through changes in Mef2c expression (Mao et al., 1999).

Finally, to confirm the essential role of ZNF335 in cerebral cortical neurogenesis, we created a brain-specific, conditional knockout of ZNF335 to bypass the embryonic lethality of a global knockout (Figure 3A). *Emx1-Cre*-mediated removal of *ZNF335* (ZNF335 CKO) (Figure S7) produced a brain with an essentially absent cortex lacking all cortical neurons at sites of *Emx1* expression (Figures 7E and 7F) (Gorski et al., 2002) and with a modest reduction in cortical size in heterozygotes compared to controls (Figure 7E). The lack of cortical plate and cortical neurons is in accordance with the essential role of ZNF335 in progenitor cells and postmitotic neurons. The small brain phenotype of the ZNF335 CKO further confirms that *ZNF335* is responsible for the severe phenotype seen in our patients and verifies *ZNF335* as a new microcephaly gene that is essential for neurogenesis and differentiation.

DISCUSSION

Here, we identify *ZNF335/NIF1* as a central regulator of mammalian neurogenesis and neuronal differentiation. A splice donor/missense mutation of *ZNF335* results in an extremely small brain in humans, and genetic ablation leads to early embryonic lethality in mice, whereas *Emx1-Cre*-driven knockout leads to virtual absence of cortical structure. Loss of ZNF335 causes premature cell-cycle exit of progenitors, precociously depleting the progenitor pool. ZNF335 is a part of a H3K4 methyltransferase complex and associates with the promoters of many key developmental genes to affect H3K4me3, as well as expression levels of target genes. A critical downstream target of ZNF335 is REST/NRSF, representing a pathway that is critical for this neurogenetic function. Beyond its effects on progenitor cell proliferation, ZNF335 also has essential effects on cell fate and cell morphology (and ultimately survival).

Despite the profound phenotype of *ZNF335* mutation in humans, the mutation that we describe is almost certainly hypomorphic. Overexpression of the human mutation can only partially rescue ZNF335 deficiency, and conditional ablation of ZNF335 in mouse cortex results in loss of essentially the entire cortex. Thus, null mutations in *ZNF335* in humans are presumably embryonically lethal as in mice, illustrating the utility of unusual, partial loss-of-function mutations in humans to elucidate essential early embryonic functions of such genes.

This study provides direct insight into the function of TrxG complex proteins in embryonic neurogenesis. The interaction of ZNF335 with proteins of the H3K4 methyltransferase complex suggests roles for ZNF335 in the regulation, targeting, or stability of the complex. Epigenetic regulation causes programming of gene expression, and specific histone methylation can further orchestrate gene regulation in a cell-type- and tissue-dependent manner. Mutations in neural-specific chromatin regulatory complexes, nBAF, have been shown to affect proliferation and are linked with microcephaly (Hoyer et al., 2012). Thus, this interaction provides a potential parallel for the broad effects of the ZNF335 mutation on human patients and the large number of genes and developmental processes altered by ZNF335 knockdown, as well as the embryonic lethality in *Znf335* null mice, especially as knockouts of other histone methyltransferases are also lethal embryonically (Glaser et al., 2009).

Loss of ZNF335 alters expression levels of many key genes, including *DLX homeobox* genes (early brain development), *Neurogenin*, *Nfib*, *Olig1*, *Math1*, *REST/NRSF*, and *Co-REST 2* (neurogenesis), among many other genes that are important for dendritic branching, cell adhesion, and signaling. Changes in these genes could explain phenotypes seen in the patients

(D) Knockdown cells show abnormal orientation based on orientation of their basal dendritic process, which is normally perpendicular to the pial surface of the brain. Rescue of shRNA-ZNF335 with WT-ZNF335 (WT-smZNF335-HA) rescues the orientation, but rescue with MUT-ZNF335 (MUT-smZNF335-HA) does not. Scale bar, 50 μm. 0.92 of total UT-control cells have apical process orientated perpendicular to pial surface (0°), 0.03 at 22.5°, and 0.04 at 337.5°. shRNA-ZNF335 knockdown cells have only 0.25 of total cells oriented at 0°, 0.13 at 22.5°, 0.11 at 45°, 0.08 at 67.5°, 0.04 at 90°, 0.04 at 270°, 0.08 at 292.5°, 0.12 at 315°, and 0.13 at 337.5°. WT-ZNF335 rescue of shRNA-ZNF335 knockdown have 0.7 cells at 0°, 0.03 at 22.5°, 0.05 at 45°, 0.3 at 67.5°, 0.04 at 90°, 0.02 at 270°, 0.03 at 292.5°, 0.07 at 315°, and 0.05 at 337.5°. MUT-ZNF335 rescue of shRNA-ZNF335 knockdown have 0.4 cells at 0°, 0.1 at 22.5°, 0.11 at 45°, 0.06 at 67.5°, 0.01 at 90°, 0.03 at 270°, 0.06 at 292.5°, 0.08 at 315°, and 0.14 at 337.5°. Data presented as proportion of total cells oriented in ±11.25° of radial direction n = 6 electroporated brains. Only matching sections were analyzed between different conditions in a double-blind manner.
See also Figure S4.

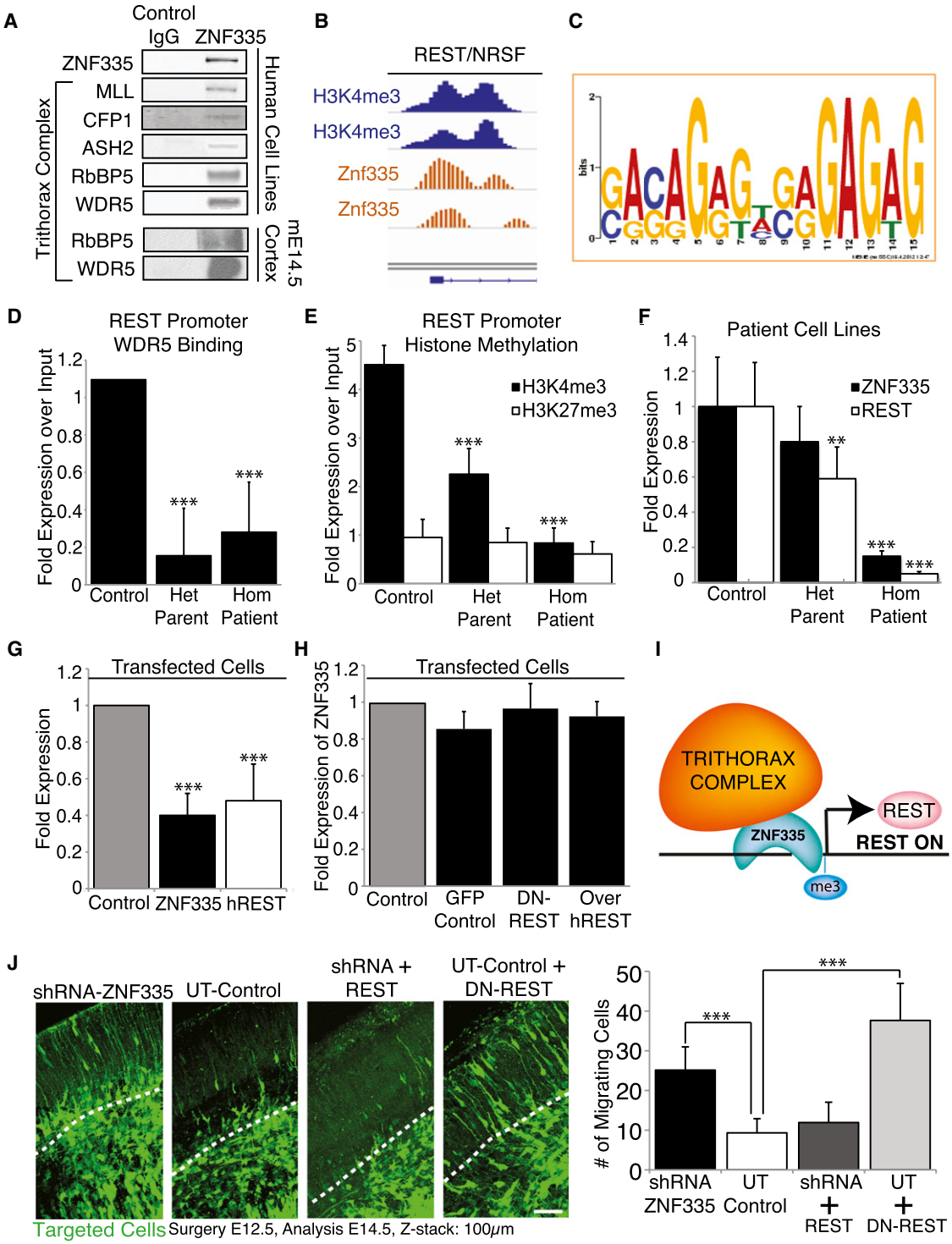

Figure 6. ZNF335 Interacts with Trithorax Complex Proteins and Is Upstream of Many Neuronal Differentiation Genes, Including REST/NRSF

(A) Blots show coimmunoprecipitation of ZNF335 with members of the trithorax complex in human HeLaS3 cell lines and mouse E14.5 cortex, indicating an interaction of ZNF335 with the histone methyltransferase complex.

(B) ZNF335 binds to promoter region of *REST/NRSF*, and binding overlaps with the H3K4me3 marks.

(C) Promoter binding consensus motif for ZNF335 with GAGAG motif that is predicted for C2H2 zinc fingers (Omichinski et al., 1997).

(D) Decreased binding of trithorax complex proteins such as WDR5 to the *REST* promoter under low levels of ZNF335. WDR5: control: 1.09 ± 0, Het parent: 0.16 ± 0.25, Hom patient: 0.28 ± 0.27; mean ± SD, $p < 0.0001$; chromatin was obtained and compiled from three different growth cultures. Two IPs were performed for each pooled set of chromatin isolated from lymphoblast cell lines, and qPCR was run in triplicates in comparison to input. All qPCR runs were normalized to *GAPDH*.

and correlate with abnormal neurogenesis evident in mouse models and account for the virtual absence of cortical neurons in the ZNF335 CKO. Genes whose expression changes upon ZNF335 deficiency could be primary targets of ZNF335 or secondary to other regulatory genes downstream of ZNF335, such as *REST/NRSF*, but reveal ZNF335 as a critical regulator of gene expression that is essential for proper neuronal development.

ZNF335 also regulates differentiation and gene transcription in postmitotic neurons. ZNF335 deficiency blocks normal expression of "canonical" neuronal marker genes, such as NeuN and Mef2C, which either could be a secondary effect of premature and improper neurogenesis or may hint at a role of ZNF335 in regulating cell identity, survival, and activity of mature neurons. ZNF335 regulates a variety of non-REST/NRSF targets that are important for the final stages of neuronal differentiation, such as genes regulating dendritic branching, and ion channels, which may suggest roles of ZNF335 in other neuron-specific transcriptional complexes.

Genetic causes of microcephaly continue to grow in diversity and include proteins involved in vesicle trafficking, mitotic spindle organization, and DNA repair (Thornton and Woods, 2009). Premature neuronal fate specification, with consequent loss of progenitor cells, could be a frequent cellular mechanism resulting in microcephaly (Lehtinen and Walsh, 2011). ZNF335 deficiency causes the additional feature of neuronal degeneration, making it strikingly different and more severe than other microcephaly syndromes, which are typically compatible with postnatal survival and, in many cases, some intellectual function. Thus, our data reveal *ZNF335* as a unique type of microcephaly gene and provide evidence of a new upstream regulator of the balance between progenitor cell division and differentiation.

EXPERIMENTAL PROCEDURES

Human Patients

Peripheral blood samples were collected from patients and unaffected family members, and mapping was performed using single-nucleotide polymorphism (SNP) arrays and microsatellite markers to narrow down the boundaries of shared homozygosity. All coding exons were sequenced in the area of homozygosity on chromosome 20q13.2 to reveal the only homozygous coding mutation in the gene *ZNF335*. All human studies were reviewed and approved by the institutional review board of the Boston Children's Hospital, the Beth Israel Deaconess Medical Center, and local institutions.

Animals

Timed pregnant CD1 and Swiss Webster dams (Charles River Laboratories and Taconic). Genetrap 1 and 2 (AY0030 and XG241) (The Genetrap Consortium). Ex utero and in utero electroporations were performed on timed pregnant E9.5–E14.5 embryos. All animal experimentation was carried out under protocols approved by the IACUCs of Harvard Medical School and Boston Children's Hospital.

Culture Systems

Primary cortical neurons were isolated from E14.5 mouse cells and dissociated by the Papain Dissociation System (Wothrington Biochem. Corp.). Cells were grown on Poly-L-Ornithine-coated plates (Sigma) in Neurobasal (GIBCO) with 0.6% glucose, B27 (GIBCO), N2 (GIBCO), 1 mM Penicillin, streptomycin, and L-glutamine and were transfected 1 hr postplating. Primary granule neurons were isolated from P5 mouse pups and grown on Poly-L-Ornithine-coated coverslips in basal medium, Eagle (GIBCO), with 10% calf serum (Hyclone), 1 mM penicillin, streptomycin, L-glutamine, and 25 mM KCl. Neurons were transfected 2 days postplating with calcium phosphate. All experiments were analyzed in a double-blind manner using an unpaired t test.

CO-IP/Mass Spectrometry

See Extended Experimental Procedures.

RNA-Sequencing

See Extended Experimental Procedures.

ChIP-Sequencing

ChIP-seq was performed on E14.5 cortical tissue with antisera against ZNF335/NIF1 (Bethyl 797, 798A). 1–10 ng of ChIP DNA was used to prepare libraries sequenced at Elim Biopharmaceuticals, Inc. Peaks were identified by MACS, and gene names were identified using custom Python scripts. All of the raw ChIP-seq data were deposited to NCBI's Gene Expression Omnibus (http://www.ncbi.nlm.nih.gov/geo/) (deposition number GSE36385). Functional characterization of genes was carried out according to the GO rules by Metacore (http://www.genego.com/genego_lp.php). See Extended Experimental Procedures.

(E) Decreased H3K4 trimethylation (marker of gene activation) of the *REST* promoter under low levels of ZNF335, but no changes in H3K27 trimethylation. H3K4me3: control: 4.5 ± 0.39, Het parent: 2.25 ± 0.53, Hom patient: 0.84 ± 0.3; H3K27me3: control: 0.95 ± 0.37; Het parent: 0.85 ± 0.29; Hom patient: 0.6, ± 0.25; $p < 0.0001$; chromatin was obtained and compiled from three different growth cultures. Two IPs were performed for each pooled set of chromatin isolated from lymphoblast cell lines, and qPCR was run in triplicates for each IP in comparison to input. All qPCR runs were normalized to *GAPDH*.

(F) qPCR measurement shows lower levels of properly spliced *ZNF335* expression and *hREST* expression in Het parent and Hom patient as compared to controls. *ZNF335* analysis was done with primers specific to only the properly spliced mRNA. Incomplete splice forms would not have been picked up with primer pairs (Exon19F, Exon 20R, Exon21R). ZNF335: Control: 1 ± 0.28, Het parent: 0.80 ± 0.21, Hom patient: 0.15 ± 0.03; hREST: control: 1 ± 0.25; Het parent: 0.59 ± 0.18; Hom patient: 0.05, ± 0.01; mean ±SD, t test compared to control, homozygous patients $p < 0.0001$; n = 9 qPCR readouts from three different growth cultures. RNA was extracted from lymphoblast cell lines. All qPCR runs were normalized to *NMYC* and *GAPDH*.

(G) Decreased levels of *hREST* expression are seen upon direct knockdown of ZNF335. Control: 1, ZNF335: 0.41 ± 0.12, $p = 0.0001$; hREST: 0.48 ± 0.20, $p = 0.0001$; mean ±SD, t test; n = 6 individual transfections of HeLa cell lines. All qPCR runs were normalized to *GAPDH*.

(H) Conversely, *ZNF335* expression is not significantly changed upon expression of dominant-negative REST (DN-REST) or overexpression of hREST (Over hREST). Control: 1.00; GFP control: 0.85 ± 0.09; DN-REST: 0.97 ± 0.14; over-hREST: 0.92 ± 0.08; mean ±SD, t test, nonsignificant; n = 3 sets of transfections of HeLa cell lines. Similar results were also seen with Hek293 cells lines (data not shown). All qPCR runs were normalized to *GAPDH*.

(I) Schematic of ZNF335 interacting with the trithorax complex to trimethylate H3K4 at the promoter of *REST* to turn on *REST* expression.

(J) Knockdown of ZNF335 leads to premature cell-cycle exit and neuronal migration in cortical plate. Addition of REST rescues the shRNA-ZNF335 phenotype and recapitulates control, whereas addition of dominant-negative REST (DN-REST) mimics ZNF335 knockdown phenotype. Dashed line represents bottom of cortical plate. Scale bar, 50 μm. shRNA-ZNF335: 25.6 ± 8.34; UT-Control: 9.32 ± 3.57; shRNA+REST rescue 11.92 ± 5.1; UT+DN-REST rescue: 37.6 ± 0.3. shRNA to UT-control: $p = 0.0001$, UT+DN-REST to UT-control: $p = 0.0001$; mean ±SD, t test; n = 3 different electroporation litters, and analysis from each litter was pooled.

See also Figure S5 and Tables S1–S7.

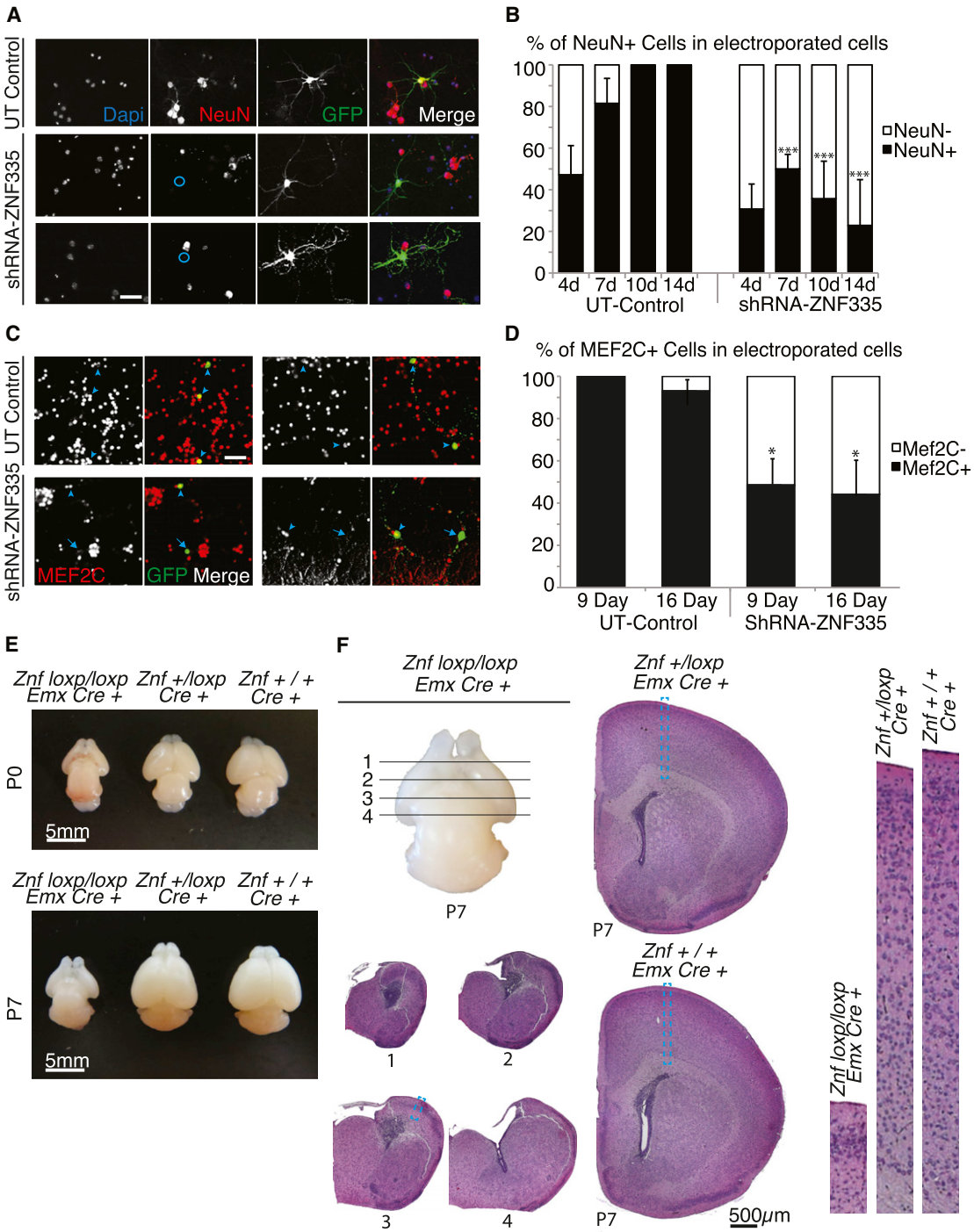

Figure 7. ZNF335 Is Essential for Neuronal Differentiation and Brain Development

(A) Knockdown of ZNF335 leads to presence of NeuN− cells (blue circles) that nonetheless have neuronal morphology in 14 day culture systems. NeuN is a marker of differentiated neurons. Scale bar, 20 μm.

(B) Quantification of NeuN+ and NeuN− cells upon knockdown of ZNF335 in short- and long-term culture shows decreased production of NeuN+ cells over long-term culture. Control NeuN+: 4 day: 48.2 ± 14.1; 7 day: 81.5 ± 12.1; 10 day: 100 ± 0.9; 14 day: 100 ± 1.5; shRNA-ZNF335 NeuN+: 4 day: 30.7 ± 12.3; 7 day: 50.0 ± 7.0; 10 day: 35.7 ± 18.1; 14 day: 22.9 ± 19.1); mean ±SD, t test, 7, 10, 14 day: $p < 0.0001$; n = 12 separate cortical neuron cultures from 12 litters.

(C) Knockdown of ZNF335 leads to Mef2C− cells (arrows), whereas UT-control shows Mef2C+ cells (arrowhead). Scale bar, 20 μm.

(D) Quantification of Mef2C+ and Mef2C− cells shows decreased production of Mef2C+ cells upon knockdown of ZNF335 in short- and long-term cultures. Control Mef2C+: 9 day: 100 ± 0.8; 16 day: 93.0 ± 8.2; shRNA-ZNF335 Mef2C+: 9 day: 48.5 ± 2.1; 16 day: 44.0 ± 15.2); mean ±SD, t test, 9 day: $p = 0.0018$, 16 day: $p = 0.008$; n = 3 separate granule cell cultures from 3 different litters.

ZNF335 CKO

Floxed allele was generated in a mixed C57/Bl6 and 129B6 background that would lead the removal of the Znf335 promoter and exons 1 and 2. See Extended Experimental Procedures.

ACCESSION NUMBERS

All of the raw ChIP-seq data were deposited to NCBI's Gene Expression Omnibus (http://www.ncbi.nlm.nih.gov/geo/) with the deposition number GSE36385 for genome-wide maps of *Znf335* localization in embryonic cortical tissue at E14.5. Microarray data were deposited with the deposition number GSE36384 (Control) and GSE36386 (knockdown).

SUPPLEMENTAL INFORMATION

Supplemental Information includes Extended Experimental Procedures, seven figures, and seven tables and can be found with this article online at http://dx.doi.org/10.1016/j.cell.2012.10.043.

ACKNOWLEDGMENTS

We thank D. Moazed, M.E. Hatten, B. Ren, D.M. Ferrero, and members of the Walsh laboratory for helpful discussions; L. Shechtman for tissue; N. Dwyer for early mapping; G. Mandel for DN-REST construct; E.E. Govek for help with cerebellar slices; K.S. Krishnamoorthy for control MRIs; and D.J. Tischfield, L.B. Hills, K.D. Atabay, P.P. Wang, J. Wortzel, D.G. Tierney, and J.M. Felie for technical assistance. This work was supported by a Stuart H.Q. and Victoria Quan Fellowship (Y.J.Y.); a NIH MSTP grant T32GM007753 (Y.J.Y. and G.D.E.); a NIH T32 HD007466 (A.E.B.); The Damon Runyon Cancer Research Foundation DRG-2042-10 (R.S.M.); HHMI Medical Research Fellows Program (E.P.W.); RO1 DK16636 (H.H.S.); NIH grants (GM058012, GM071004, and CA118487) (Y.S.); grants from the NINDS (RO1 NS032457 and R01 NS35129); and the Manton Center for Orphan Disease Research (C.A.W.). C.A.W. is an Investigator of the Howard Hughes Medical Institute. The content is solely the responsibility of the authors and does not necessarily represent the official views of the NINDS or the NIH.

Received: March 15, 2012
Revised: July 27, 2012
Accepted: October 17, 2012
Published: November 21, 2012

REFERENCES

Ang, Y.S., Tsai, S.Y., Lee, D.F., Monk, J., Su, J., Ratnakumar, K., Ding, J., Ge, Y., Darr, H., Chang, B., et al. (2011). Wdr5 mediates self-renewal and reprogramming via the embryonic stem cell core transcriptional network. Cell *145*, 183–197.

Ballas, N., Grunseich, C., Lu, D.D., Speh, J.C., and Mandel, G. (2005). REST and its corepressors mediate plasticity of neuronal gene chromatin throughout neurogenesis. Cell *121*, 645–657.

Bannister, A.J., and Kouzarides, T. (2011). Regulation of chromatin by histone modifications. Cell Res. *21*, 381–395.

Barkovich, A.J., Moore, K.R., Jones, B.V., Vezina, G., Koch, B.L., Raybaud, C., Grant, P.E., Blaser, S.I., Hedlund, G.L., and Illner, A. (2007). Diagnostic Imaging: Pediatric Neuroradiology, First Edition (Salt Lake City, UT: Amirsys).

Bernstein, B.E., Kamal, M., Lindblad-Toh, K., Bekiranov, S., Bailey, D.K., Huebert, D.J., McMahon, S., Karlsson, E.K., Kulbokas, E.J., III, Gingeras, T.R., et al. (2005). Genomic maps and comparative analysis of histone modifications in human and mouse. Cell *120*, 169–181.

Cartegni, L., Chew, S.L., and Krainer, A.R. (2002). Listening to silence and understanding nonsense: exonic mutations that affect splicing. Nat. Rev. Genet. *3*, 285–298.

Chong, J.A., Tapia-Ramírez, J., Kim, S., Toledo-Aral, J.J., Zheng, Y., Boutros, M.C., Altshuller, Y.M., Frohman, M.A., Kraner, S.D., and Mandel, G. (1995). REST: a mammalian silencer protein that restricts sodium channel gene expression to neurons. Cell *80*, 949–957.

Dredge, B.K., and Jensen, K.B. (2011). NeuN/Rbfox3 nuclear and cytoplasmic isoforms differentially regulate alternative splicing and nonsense-mediated decay of Rbfox2. PLoS ONE *6*, e21585.

Fietz, S.A., and Huttner, W.B. (2011). Cortical progenitor expansion, self-renewal and neurogenesis-a polarized perspective. Curr. Opin. Neurobiol. *21*, 23–35.

Fisher, C.L., and Fisher, A.G. (2011). Chromatin states in pluripotent, differentiated, and reprogrammed cells. Curr. Opin. Genet. Dev. *21*, 140–146.

Garapaty, S., Xu, C.F., Trojer, P., Mahajan, M.A., Neubert, T.A., and Samuels, H.H. (2009). Identification and characterization of a novel nuclear protein complex involved in nuclear hormone receptor-mediated gene regulation. J. Biol. Chem. *284*, 7542–7552.

Glaser, S., Lubitz, S., Loveland, K.L., Ohbo, K., Robb, L., Schwenk, F., Seibler, J., Roellig, D., Kranz, A., Anastassiadis, K., and Stewart, A.F. (2009). The histone 3 lysine 4 methyltransferase, Mll2, is only required briefly in development and spermatogenesis. Epigenetics Chromatin *2*, 5.

Gorski, J.A., Talley, T., Qiu, M., Puelles, L., Rubenstein, J.L., and Jones, K.R. (2002). Cortical excitatory neurons and glia, but not GABAergic neurons, are produced in the Emx1-expressing lineage. J. Neurosci. *22*, 6309–6314.

Hoyer, J., Ekici, A.B., Endele, S., Popp, B., Zweier, C., Wiesener, A., Wohlleber, E., Dufke, A., Rossier, E., Petsch, C., et al. (2012). Haploinsufficiency of ARID1B, a member of the SWI/SNF-a chromatin-remodeling complex, is a frequent cause of intellectual disability. Am. J. Hum. Genet. *90*, 565–572.

Isken, O., and Maquat, L.E. (2007). Quality control of eukaryotic mRNA: safeguarding cells from abnormal mRNA function. Genes Dev. *21*, 1833–1856.

Johnson, R., Teh, C.H., Kunarso, G., Wong, K.Y., Srinivasan, G., Cooper, M.L., Volta, M., Chan, S.S., Lipovich, L., Pollard, S.M., et al. (2008). REST regulates distinct transcriptional networks in embryonic and neural stem cells. PLoS Biol. *6*, e256.

Lehtinen, M.K., and Walsh, C.A. (2011). Neurogenesis at the brain-cerebrospinal fluid interface. Annu. Rev. Cell Dev. Biol. *27*, 653–679.

Lessard, J.A., and Crabtree, G.R. (2010). Chromatin regulatory mechanisms in pluripotency. Annu. Rev. Cell Dev. Biol. *26*, 503–532.

Lui, J.H., Hansen, D.V., and Kriegstein, A.R. (2011). Development and evolution of the human neocortex. Cell *146*, 18–36.

Ma, D.K., Marchetto, M.C., Guo, J.U., Ming, G.L., Gage, F.H., and Song, H. (2010). Epigenetic choreographers of neurogenesis in the adult mammalian brain. Nat. Neurosci. *13*, 1338–1344.

Mahmood, S., Ahmad, W., and Hassan, M.J. (2011). Autosomal Recessive Primary Microcephaly (MCPH): clinical manifestations, genetic heterogeneity and mutation continuum. Orphanet J. Rare Dis. *6*, 39.

Mao, Z., Bonni, A., Xia, F., Nadal-Vicens, M., and Greenberg, M.E. (1999). Neuronal activity-dependent cell survival mediated by transcription factor MEF2. Science *286*, 785–790.

(E) ZNF335 CKO (*Znfloxp/loxp;Emx1Cre+*) shows decreased formation of cerebral cortex in all areas where *Emx1-Cre* is expressed and a small lateral cortex in areas where *Emx1-cre* is reduced or turned on later at both P0 and P7.
(F) H&E stain of coronal brain sections of ZNF335 CKO (*Znfloxp/loxp;Emx1Cre+*), ZNF335-Het (*Znf+/loxp;Emx1Cre+*), and ZNF335-WT (*Znf+/+;Emx1Cre+*) shows that ZNF335 CKO lack almost all cortical structure and cortical neurons. The loss of cortical brain structure leads to the formation of a small brain with a thin sheath of tissue and enlarged ventricles. Blue dashed box represents enlarged cortical sections (right).
See also Figures S6 and S7.

Mochida, G.H. (2009). Genetics and biology of microcephaly and lissencephaly. Semin. Pediatr. Neurol. *16*, 120–126.

Molyneaux, B.J., Arlotta, P., Menezes, J.R., and Macklis, J.D. (2007). Neuronal subtype specification in the cerebral cortex. Nat. Rev. Neurosci. *8*, 427–437.

Ng, R.K., and Gurdon, J.B. (2008). Epigenetic inheritance of cell differentiation status. Cell Cycle *7*, 1173–1177.

Omichinski, J.G., Pedone, P.V., Felsenfeld, G., Gronenborn, A.M., and Clore, G.M. (1997). The solution structure of a specific GAGA factor-DNA complex reveals a modular binding mode. Nat. Struct. Biol. *4*, 122–132.

Papp, B., and Müller, J. (2006). Histone trimethylation and the maintenance of transcriptional ON and OFF states by trxG and PcG proteins. Genes Dev. *20*, 2041–2054.

Paro, R., Strutt, H., and Cavalli, G. (1998). Heritable chromatin states induced by the Polycomb and trithorax group genes. Novartis Found Symp. *214*, 51–61.

Schoenherr, C.J., and Anderson, D.J. (1995). Silencing is golden: negative regulation in the control of neuronal gene transcription. Curr. Opin. Neurobiol. *5*, 566–571.

Schuettengruber, B., Martinez, A.M., Iovino, N., and Cavalli, G. (2011). Trithorax group proteins: switching genes on and keeping them active. Nat. Rev. Mol. Cell Biol. *12*, 799–814.

Shen, Y., Yue, F., McCleary, D.F., Ye, Z., Edsall, L., Kuan, S., Wagner, U., Dixon, J., Lee, L., Lobanenkov, V.V., and Ren, B. (2012). A map of the cis-regulatory sequences in the mouse genome. Nature *488*, 116–120.

Sun, Y.M., Greenway, D.J., Johnson, R., Street, M., Belyaev, N.D., Deuchars, J., Bee, T., Wilde, S., and Buckley, N.J. (2005). Distinct profiles of REST interactions with its target genes at different stages of neuronal development. Mol. Biol. Cell *16*, 5630–5638.

Thornton, G.K., and Woods, C.G. (2009). Primary microcephaly: do all roads lead to Rome? Trends Genet. *25*, 501–510.

Zheng, J.N., Ma, T.X., Cao, J.Y., Sun, X.Q., Chen, J.C., Li, W., Wen, R.M., Sun, Y.F., and Pei, D.S. (2006). Knockdown of Ki-67 by small interfering RNA leads to inhibition of proliferation and induction of apoptosis in human renal carcinoma cells. Life Sci. *78*, 724–729.

Cell

EXTENDED EXPERIMENTAL PROCEDURES

Supplemental Clinical Information

The overall pedigree is one of a family of Israeli Arab ancestry with multiple loops of consanguinity, consisting of two main nuclear branches.

Nuclear Family A

This family includes parents who are first cousins of Israeli Arab ancestry and multiple affected children. They first came to attention with the birth of male twin infants, Patients 7 & 8. Prenatal ultrasound examination at 28 weeks gestation revealed microcephaly in both feti and the twins were delivered by cesearean section at 35 weeks for intra uterine growth restriction. At birth both children were noted to have severe microcephaly, dysmorphic facial features including prominent nasal bridge, arthrogryposis, choanal atresia and bilateral cataracts. Postnatal renal ultrasound was normal. Birth weight for patient 7 was 1395 g and he was hospitalized at 8 weeks old with hypothermia. Sepsis work up was negative but he died at 3 months old. The second twin's birth weight was 1700 g and he was hospitalized at 2 months old with pneumonia and hypothermia. By age 3 months his head circumference was 27.5 cm (−9.0 Standard Deviations) and length was 51 cm (−4.3 Standard Deviations). Physical exam revealed the low sloping forehead, micrognathia, prominent helicies, bilateral simian creases, flexion contractures of both hands with overriding fingers, dorsiflexion of both feet with overriding toes and increased tone and spasticity. MRI of the brain revealed obvious microcephaly with a cortex with normal thickness, very few sulci and no observable basal ganglia, absence of the corpus callosum, enlarged ventricles, lack of olfactory sulci, markedly reduced white matter volume, delayed myelination and hypoplastic cerebellar hemispheres, vermis and brainstem. This family also had another son and two daughters with similar features. All died by age 18months old with the exception of a female, who was still living at age 5 years old with severe psychomotor retardation and dysmorphisms. The parents were clinically normal, but available data on the parents is limited, so that mild phenotypes such as borderline intelligence cannot be ruled out.

Nuclear Family B

This family is related to the previous family (A) as the father of Family A is siblings with the mother of Family B. Also, the mother of Family A is first cousin once removed to the father of Family B. The parents in this nuclear family B are related as first cousins once removed. This nuclear family includes two affected males with similar clinical features to the previously described children and there are also two unaffected siblings, a male and a female. The first affected male died at 2.5 months old. The second affected male, patient 5, had negative genetic workup including a karyotype and FISH for 17p13.3 (Miller-Dieker syndrome). Post-mortem Histology: Lissencephalic cortex with reduced white matter and abnormal lamination lacking the normal six layers. Grey-white matter boundary is preserved but signs of cell degeneration, abnormal cell orientation, and gliosis. Cerebellum showed severely reduced molecular layer external granule layer, molecular layer, and internal granule layer. Bergmann glia was present in the Purkinje cell layer, and there were few Purkinje cells, with abnormal polarity, and cell-sparse internal granule layer.

Human Patients

Genome-wide Linkage Scans

We collected peripheral blood samples from the affected children and their parents and other family members after obtaining written informed consent according to the protocols approved by the participating institutions. All human studies were reviewed and approved by the institutional review board of the Boston Children's Hospital, the Beth Israel Deaconess Medical Center and the local institutions. A total of 22 individuals (indicated with an asterisk in Figure 1A) were genotyped via Affymetrix 10K Xba121, Affymetrix 250K Nsp, Affymetrix 250 Sty, and Affymetrix 5.0. One block of homozygosity on chromosome 20q13.12 (Figure 2A) emerged as being shared by all affected individuals (shaded in in Figure 1A). To refine the region of homozygosity, samples underwent a microsatellite genome-wide linkage screen using ~400 markers in the ABI linkage mapping set MD v2.5 at ~10cM average density (Applied Biosystems). Fine mapping was done using polymorphic microsatellite markers from the ABI linkage mapping set HD v2.5 at a 5cM average density (Applied Biosystems) and additional microsatellite markers identified using the UCSC Human Genome Browser. The candidate interval was defined by markers D20S838-6 and D20S197-12 giving an interval of a 2MB locus. Singlepoint and multipoint LOD scores were calculated using Allegro, assuming a recessive mode of disease inheritance, full penetrance and a disease allele frequency of 0.0001. The LOD score is 4.538 ($p < 0.0001$).

DNA Sequence Analysis

Sequence analysis of the coding exons of the 40 protein-coding RefSeq genes in the linked interval (Figure 2A) revealed a candidate mutation in *ZNF335* (*Zinc Finger Protein 335* also known as *NIF1*, *NRC Interacting Factor 1.* Location 20q13.12, MIM 610825, NM 022095). The change was a c.3332g>a. All affected children were homozygous for this change and the parents, who were obligate carriers, were all heterozygous.

Sequencing of ZNF335 in Controls

Coding *ZNF335* exons and at least 50 basepairs of flanking sequence were PCR amplified and submitted for Sanger capillary electrophoresis (Polymorphic DNA Technologies) in accordance with standard methods. Samples included 100 neurologically normal patients. We also reviewed whole exome sequencing for 200 unaffected Arabic control patients and 2500 European control patients.

Immunostaining

Paraffin sections (5uM) of brains were dehydrated and subjected to antigen retrieval with Antigen Unmasking Solution (Vector), followed by blocking (PBS/5% serum), permeabilization (0.04% Tween20), and antibody incubation. Alternatively, cryosections (8um-16um) and vibratome sections (50um-200um) were permeabilized (0.04% Tween20, 0.1% Triton X-100), blocked, and incubated with antibodies (24h-48h). For the migration assays, slices were immunostained with rabbit anti-GFP antibody (Invitrogen) and mouse anti-Calbindin antibody (Swant). All samples were counterstained with Hoechst 33258 (Sigma). All images were taken with Zeiss 510 or Zeiss 700. For morphology analysis and images of thick sections (>16um), Z-stack images were obtained using Zeiss 510. Sections were morphologically matched before comparing experimental to control conditions. Data analysis was performed through a double-blind method using ImageJ Software. Confocal imaging was performed at the BIDMC core facility.

Antibodies

Znf335/Nif1 (797, 798A, IHC specific, 2000, Bethyl); BrdU (250, AbD Serotec); Ki67 (250, Abnova); Vimentin 4A4 (500, Assay Designs); GLAST (250, Chemicon); NeuN (4000, Millipore); FLAG (500, Sigma); GFP (500, Abcam); ASH2 (500, Bethyl Laboratories); MLL/HRX (1000, Millipore); RbBP5 (500, Bethyl Laboratories); SETD1A (200, Novus Biologicals); CGBP (200 Gene Tex); MATR3 (Aviva Systems Biology); WDR5 (200 Milipore); FoxP1 (500 Abcam); Cux1/CDP (500 Santa Cruz).

X-Gal Staining

Embryos and adult animals were perfused with 4% PFA and brains were sectioned (50um) then stained with 1g/L X-Gal (Invitrogen).

FACS Sort

Tissues and cells were dissociated using either the Papain Dissociation System (Worthington Biochem Corp) or Neurocult (Stem Cell). Dissociated cells were sorted for GFP using FACSVantage under lowest sustainable pressure. Cells were only used if re-sort verification of > 95% pure GFP-positive population was obtained.

Microarray

RNA was isolated with RNeasy Mini Kit (QIAGEN), and processed with the Microarray Core Facility (DFCI) using Mouse 430.2 microarray chips. Gene expression was analyzed using DChip Software. All of the raw microarray data were deposited to NCBI's Gene Expression Omnibus (http://www.ncbi.nlm.nih.gov/geo/) under deposition number GSE363864 and GSE36386.

Neurospheres

E19.5 and E12.5 mouse cortex was dissected in sterile HBSS and dissociated by the papain Dissociation System (Worthington Biochem Corp). Suspension cultures were transfected with either Lipofectamine 2000 (Invitrogen) or Calcium Phosphate (Clontech). 24hrs post, cells were dissociated using Neurocult (Stemcell) and FACS sort was used to isolate and plate only GFP-positive (transfected) cells and cells were plated at 56K/cm2.

In Utero Electroporations

Plasmid DNA suspended at 1ug/ul in ddH2O was stained with DNA Loading Dye (Invitrogen) and microinjected into the lateral ventricle of developing embryos by eye or using ultrasound guidance (Olson et al., 2006). Moms were allowed to recover and embryos were harvested at different stages. All animal surgical experiment was carried out under protocols approved by the IACUCs of Harvard Medical School, and Children's Hospital Boston. For cell cycle analysis 70 ug BrdU/g body weight was administered via an intraperitoneal injection at 32 hr post electroporation and animals were examined at 48 hr post electroporation. Analysis were done on serial 5-16um paraffin sections and only analyzed between sections in matching brain regions and well as matching medial to lateral orientation of cells between knockdown and control. Rescues were performed by co-electroporating the expression constructs at the same time as the knockdown and control constructs while keeping the amount of shRNA-ZNF335 and UT-Control constructs equal to non-rescue experiments.

Cerebellar Slices

For ex vivo cerebellar electroporations, P8 cerebella were dissected, soaked in endotoxin free plasmid DNA suspended at 2 μg/μl in complete Hanks Balance Salt Solution (HBSS), transferred to a CUY520-P5 Platinum Block Petridish Electrode (Protech International) and electroporated with an ECM 830 square wave electroporator (BTX Genetronics) at 80 V, 5 pulses, 50 ms pulse, and 500 ms interval. Electroporated cerebella were embedded in 3% low melting point agarose in HBSS, and 250 μm coronal or sagittal cerebellar slices were prepared using a VT1000S Vibratome (Leica Microsystems). Slices were transferred to Millicell tissue culture inserts (Millipore) and cultured in Basal Medium Eagle supplemented with 2 mM L- glutamine, 0.5% glucose, 1x ITS (Sigma), and 50 U/ml Penicillin-Streptomycin, at the air-medium interface. In experiments where proliferation was assayed, 25 μM EdU was added to the culture medium at 24 hr in culture. Slices were fixed after 48 hr and 72 hr in culture using ice-cold 4% paraformaldehyde/4% sucrose/1x PBS for two hours.

Northern Blot

Mouse probes were generated from mouse *Zfp335* cDNA (Clone ID 6848450, Open Biosystems) to contain a 960-bp sequence corresponding to nucleotide position 2,227–3,231 of the cDNA or a 560-bp sequence corresponding to nucleotide position 3,922-4,475 of the cDNA. Human probes were generated from human *ZNF335* cDNA (Clone ID 5285131, Open Biosystems) to contain a 446-bp sequence corresponding to nucleotide position 2,073-2,519 of the cDNA or a 584-bp sequence corresponding to nucleotide position 2,587-3,171 of the cDNA. Probes were generated using pCRII (Invitrogen), Northern blots were done with RNA extracted from human patient lymphocytes or using Mouse Embryo MTN Blot (Clontech), Human 12-Lane MTN Blot (Clontech), and Human Fetal MTN Blot II (Clontech).

Western Blot

Bands were either detected with Pico-ECL or Femto-ECL detection kits (Invitrogen), or with the Odyssey Infrared Imaging System (Li-Cor Biosciences). Quantitation was achieved with Odyssey Infrared Imaging System (Li-Cor Biosciences).

CO-IP/Mass Spectrometry

HeLaS3 Co-IP: Protein complex of ZNF335 was isolated and purified as described previously (Ogawa et al., 2002). Briefly, nuclear extract was prepared from 10L of HeLa S3 cells stably expressing Flag-ZNF335 fusion protein. ZNF335 complex was purified using anti-Flag M2 mAb-conjugated agarose beads (Sigma) in a buffer containing 20cmM Tris-HCl, pH 7.9, 100mM KCl, 5cmM $MgCl_2$, 10% glycerol, 1cmM phenylmethylsulphonyl fluoride (PMSF), 0.1% Nonidet P40, and 10cmM 2-mercaptoethanol.

Mouse E14.5 Co-IP: Nuclear lysates of mouse E14.5 brains form 20 litters were pooled for analysis following the published methods (Chen et al., 2009). IP material was separated by 4%–12% gradient SDS–polyacrylamide-gel electrophoresis (SDS–PAGE) and stained with Coomassie blue. Protein bands were excised and analyzed by mass spectrometry at the Harvard Medical School Taplin Biological Mass Spectrometry Facility.

RNA-Sequencing Analysis

EBV-transformed lymphoblastoid cell lines from Het Parents (LIS-4411), Homozygous Patients (LIS-4421), and 7 unrelated individuals were cultured in RPMI-1640 media supplemented with 10% FBS and penicillin-streptomycin. Approximately 80 million cells from each cell line were fractionated with Cell Fractionation Buffer (PARIS kit, Ambion) to separate cytoplasmic and nuclear lysates. RNA was purified from the lysates with the mirVana PARIS kit (Ambion). RNA was DNase treated (QIAGEN) and cleaned-up (RNeasy, QIAGEN). Cytoplasmic and nuclear RNA yields and integrity were confirmed on a NanoDrop spectrophotometer (Thermo Scientific) and RNA 6000 Bioanalyzer (Agilent). Separation of cytoplasmic from nuclear RNA was confirmed by electrophoresis (unspliced rRNA visible only in nuclear fraction, data not shown), and by qPCR for U1 snRNA enrichment in the nuclear fraction (data not shown).

PolyA-tailed mRNA from cytoplasmic RNA fractions was purified with two rounds of polyA-selection: a first purification with Poly(A)Purist MAG (Life technologies), and a second purification with the Oligotex mRNA kit (QIAGEN). Absence of rRNA following polyA(pA)-selection was confirmed by RNA 6000 Bioanalyzer. About 200-400ng of pA-cytoplasmic RNA was fragmented using RNaseIII as specified in the SOLiD Whole Transcriptome Analysis Kit (Applied Biosystems). Initial sequencing of Het Parent (LIS-4411), Homozygous Patient (LIS-4421) and 3 unrelated controls revealed a strong bias in the protocol's enzymatic fragmentation, leading to reduced library diversity. In a subsequent experiment we employed an alternative more random RNA heat-fragmentation method. pA-cytoplasmic RNA from homozygous patient (LIS-4421) and 7 unrelated controls was heat fragmented by incubation with 1ul RNase III reaction buffer (SOLiD, Applied Biosystems) in a 10ul volume for 10 min. at 95°C to obtain a more random fragmentation. Heat-fragmented RNA was end-repaired with 1ul T4 PNK (10U/ul) and 1ul ATP (10mM) in a 12ul volume, incubated for 30 min. at 37°C. The RNA was cleaned-up with the RiboMinus Concentration Module (Invitrogen).

Fragmentation by both methods was confirmed with the RNA 6000 Bioanalyzer chip. Barcoded sequencing libraries preserving strand-information were prepared with the SOLiD Whole Transcriptome Analysis Kit (Applied Biosystems). RNaseIII-fragmented and heat-fragmented libraries were sequenced to an average depth of 56 million and 70 million reads per sample, respectively, on the SOLiD version 3 Plus sequencing system.

Sequencing reads were spectrally corrected using the SOLiD Accuracy Enhancer Tool (Applied Biosystems) and mapped with standard settings using Bioscope software v1.3 (Applied Biosystems) to the human genome reference (hg19) and splice-junctions obtained from the UCSC Genes annotation track (Kent et al., 2002). All differential gene and intron expression analyses were performed with sequencing data from the heat-fragmented libraries. The number of uniquely mapped reads per gene and per-intron were counted using htseq-count (Anders, 2007) and the RefSeq gene and intron annotations. Differential gene and intron expression analysis were performed with DESeq (Anders and Huber, 2010).

Consensus Sequence Motif Analysis

Consensus sequencing binding motif was defined using the Meme and Dreme softwares (meme.ncbr.net) and our ChIP-Seq data sets. Promoter sequences with ZNF335-binding peaks were utilized to generate the binding motif, and analyzed over controls using promoter sequences of genes that did not exhibit ZNF335-binding.

ChIP-Sequencing Analysis

Embryonic cortical tissue was isolated from mouse embryos at E14.5. Cross-linking, chromatin isolation, sonication and immunoprecipitation using two distinct rabbit polyclonal antibody raised against Znf335/Nif1 were performed as previously described (Barrera et al., 2008; Renthal et al., 2009; Tsankova et al., 2004). Sequencing libraries were generated from 1-10 ng of ChIP DNA by adaptor ligation, gel-purification and 18 cycles of PCR, according to standard Illumina protocols (http://www.illumina.com/support/documentation.ilmn). Gel-purified amplified ChIP DNA and control DNA between 175 and 400 bp were sequenced on the Illumina Genome Analyzer II platform according to the manufacturer's specifications by ELIM Biopharmaceuticals (http://www.elimbio.com/) to generate 36-bp reads.

ChIP-Seq Data Analysis

Sequence reads were aligned to the mouse reference genome (mm9) using Bowtie (Langmead et al., 2009). Only reads which mapped uniquely to the genome were retained. Table S7A shows a summary of the alignment and mapping statistics. The peak calling program MACS (Zhang et al., 2008) was used to identify peaks with the mapped reads. Table S7B shows the parameters used when running MACS (mainly default parameters). Enriched intervals were identified by comparison of the mean fragment count in 1-kb windows against a sample-specific expected distribution obtained by sequencing the control DNA. Enriched intervals, or peaks, were normalized based on the total number of reads per ChIP-seq library (reads per million) and mapped to their corresponding genomic position using custom Python scripts.

All of the raw ChIP-seq data were deposited to NCBI's Gene Expression Omnibus (http://www.ncbi.nlm.nih.gov/geo/) with the deposition number GSE36386 for genome-wide maps of *Znf335* localization in embryonic cortical tissue at E14.5.

Ontological, Pathway, and Network Analysis

Ontological analysis used Gene Ontology (GO) categories to determine processes or functional categories that were represented in both ChIP data sets or commonly expressed in the short and long-term microarray data sets, as described previously (Ashburner et al., 2000) using the GeneGo functional annotation module of Metacore (http://www.genego.com/genego_lp.php). This analysis determined the number of genes in a category present in the i) ChIP-seq, ii) microarray or iii) RNA-seq data and the number of chromatin-binding or expression changes that would be part of that category by random chance given the number of commonly expressed genes. Statistical significance of each process or category was established by p-value (p-value < 0.01). Only the processes or categories which passed this threshold were grouped by common function are represented for each genome-wide data set (Figure 6D).

ChIP-qPCR

Analysis were done on human lymphoblast cell lines harvested on the exponential growth stage. ChIP-qPCR was performed following published methods (Kim et al., 2010), 3ug of antibodies were used for each ChIP. Antibodies used were: H3K4me3 (Millipore), H3K27me3 (Millipore), WDR5 (Abcam), MLL (Millipore).

ChIP-qPCR Promoter Primer Sequences

AIMP1: forward, TTAGTGCACCAGACGCTGCATTTC; reverse, TATGTCCTTTCGTGGCCAGTTTGG. Rbbp5: forward, TTCTACCTCACCTACATGTTCCCG; reverse, CTCCGAAGACTTTCGGCCTTAGAA. Caprin1: forward, AACGATTTCGCCTGAAGGACCCTA; reverse, ACTTAGCCAGCCAGCAGC. Pes1: forward, CCTGGACTTGTACAGGCATCTCAT; reverse, TTCTTCTTCTCAAGGCCTCCCATC. Pdap1: forward, AACACATACCGGAAGCTCCT; reverse, AGCGGCTCTGGAATTCTATACAGG. Hspa9: forward, CGCAATTTATCCCGTGTGACCTTG; reverse, AGCATGATGGTTGGAGAAAGCCTG. Taf9: forward, TCATCGAAAGCCAGGTAACCAGTG; reverse, AGGATGTTCGGAAGCAACATGGTC. Suds3: forward, ACACTGCTAGGCAGACGG; reverse, TCTCCAGCTCTTCATCCTCCT. Dand5: forward, GGAACCCAGCTGGTCTGAATTTAC; reverse, AAGCAGGCACAGAAGAGTGGATAG. REST/NRSF: forward, TGCTGTGATTACCTGGTCGGTGAA; reverse, TCTTCGAGCTCTTGCCTTTGTCCT.

Gene Expression Validation

hREST F&R: Mm0083268_m1 (Taqman); GAPDH-F: 5′CCAAGGTCATCCATGACAAC; GAPDH-R: 5′GGCCATCCACAGTCTTCTG; ZNF335-F: 5′GTCTGTCACACAGGCTCAAC; ZNF335-R: 5′GCACTGGTCTCGTCTGTACCAA; ZNF-Exon19F: GCTGAGATGGAGAGTCACAAG; ZNF-Exon20R; CTGCACTGGCTACACTGG; ZNF-Exon21R; TGGATGTGGAACTTGAGGTG.

shRNA Constructs

shRNA were expressed using a modified pSilencer1.0 construct. shRNA-ZNF335: CAGCAGCTTCCTCAACAAAGTTCAAGAGACTTTCTTGAGGAAGCTGCTC; UT-CONTROL: CTGCTGCATCGTCTACTAAGTTCAAGAGACTTAGTAGACGATGCAGCAG.

Znf335 CKO Mouse Generation

Design: In mouse, the *ZNF335* gene is called *Zfp335* for Zinc finger Protein 335. A Loxp (L83) site and a FNFL (Frt-Neo-Frt-Loxp) cassette were engineered to flank promoter and exon1/2 (2kb) of the Zfp335 allele to generate "L83/FNFL" Zfp335 allele on a Bacterial Artificial Chromosome (BAC). A gene targeting vector was constructed by retrieving the 2kb short homology arm (5′ to L83), the floxed sequence containing promoter and exon1/2, the FNFL cassette, and the 5kb long homology arm (end of FNFL to 3′) into a plasmid vector carrying a DTA (Diphtheria Toxin Alpha chain) negative selection marker. The FNFL cassette conferred G418

resistance during gene targeting in PTL1 (129B6 hybrid) ES cells and the DTA cassette provided an autonomous negative selection to reduce the random integration event (Precision Targeting). Several targeted ES cells were identified. These targeted ES cells were injected into C57BL/6 blastocysts to generate chimeric mice. Male chimeras should be bred to homozygous ACTB(Flpe/Flpe) females (in C57BL/6 background, Jackson labs) to transmit the floxed ZFP335 allele (L83/FL146 allele with neo cassette removed by Fple recombinase) Mice carrying floxed ZFP335 allele were crossed to Emx1-Cre mice (in C57BL/6 mice, Jackson labs) to generate ZFP335 conditional knockout study. The mice are maintained on a mixed C57/Bl6 and 129B6 background. For histological analysis, brains were perfused with PBS and then followed by 4% PFA before paraffin embedding and sectioning.

SUPPLEMENTAL REFERENCES

Adams, N.C., Tomoda, T., Cooper, M., Dietz, G., and Hatten, M.E. (2002). Mice that lack astrotactin have slowed neuronal migration. Development *129*, 965–972.

Anders, S. (2007). HTSeq: Analysing high-throughput sequencing data with Python (Free Software Foundation, Inc.).

Anders, S., and Huber, W. (2010). Differential expression analysis for sequence count data. Genome Biol. *11*, R106.

Ashburner, M., Ball, C.A., Blake, J.A., Botstein, D., Butler, H., Cherry, J.M., Davis, A.P., Dolinski, K., Dwight, S.S., Eppig, J.T., et al.; The Gene Ontology Consortium (2000). Gene ontology: tool for the unification of biology. Nat. Genet. *25*, 25–29.

Barrera, L.O., Li, Z., Smith, A.D., Arden, K.C., Cavenee, W.K., Zhang, M.Q., Green, R.D., and Ren, B. (2008). Genome-wide mapping and analysis of active promoters in mouse embryonic stem cells and adult organs. Genome Res. *18*, 46–59.

Chen, C., Jin, J., James, D.A., Adams-Cioaba, M.A., Park, J.G., Guo, Y., Tenaglia, E., Xu, C., Gish, G., Min, J., and Pawson, T. (2009). Mouse Piwi interactome identifies binding mechanism of Tdrkh Tudor domain to arginine methylated Miwi. Proc. Natl. Acad. Sci. USA *106*, 20336–20341.

Kent, W.J., Sugnet, C.W., Furey, T.S., Roskin, K.M., Pringle, T.H., Zahler, A.M., and Haussler, D. (2002). The human genome browser at UCSC. Genome Res. *12*, 996–1006.

Kim, T.K., Hemberg, M., Gray, J.M., Costa, A.M., Bear, D.M., Wu, J., Harmin, D.A., Laptewicz, M., Barbara-Haley, K., Kuersten, S., et al. (2010). Widespread transcription at neuronal activity-regulated enhancers. Nature *465*, 182–187.

Langmead, B., Trapnell, C., Pop, M., and Salzberg, S.L. (2009). Ultrafast and memory-efficient alignment of short DNA sequences to the human genome. Genome Biol. *10*, R25.

Morrison, M.E., and Mason, C.A. (1998). Granule neuron regulation of Purkinje cell development: striking a balance between neurotrophin and glutamate signaling. J. Neurosci. *18*, 3563–3573.

Nagata, I., Ono, K., Kawana, A., and Kimura-Kuroda, J. (2006). Aligned neurite bundles of granule cells regulate orientation of Purkinje cell dendrites by perpendicular contact guidance in two-dimensional and three-dimensional mouse cerebellar cultures. J. Comp. Neurol. *499*, 274–289.

Ogawa, H., Ishiguro, K., Gaubatz, S., Livingston, D.M., and Nakatani, Y. (2002). A complex with chromatin modifiers that occupies E2F- and Myc-responsive genes in G0 cells. Science *296*, 1132–1136.

Olson, E.C., Kim, S., and Walsh, C.A. (2006). Impaired neuronal positioning and dendritogenesis in the neocortex after cell-autonomous Dab1 suppression. J. Neurosci. *26*, 1767–1775.

Renthal, W., Kumar, A., Xiao, G., Wilkinson, M., Covington, H.E., III, Maze, I., Sikder, D., Robison, A.J., LaPlant, Q., Dietz, D.M., et al. (2009). Genome-wide analysis of chromatin regulation by cocaine reveals a role for sirtuins. Neuron *62*, 335–348.

Smeyne, R.J., Chu, T., Lewin, A., Bian, F., Sanlioglu, S., Kunsch, C., Lira, S.A., and Oberdick, J. (1995). Local control of granule cell generation by cerebellar Purkinje cells. Mol. Cell. Neurosci. *6*, 230–251.

Tsankova, N.M., Kumar, A., and Nestler, E.J. (2004). Histone modifications at gene promoter regions in rat hippocampus after acute and chronic electroconvulsive seizures. J. Neurosci. *24*, 5603–5610.

Zhang, Y., Liu, T., Meyer, C.A., Eeckhoute, J., Johnson, D.S., Bernstein, B.E., Nusbaum, C., Myers, R.M., Brown, M., Li, W., and Liu, X.S. (2008). Model-based analysis of ChIP-Seq (MACS). Genome Biol. *9*, R137.

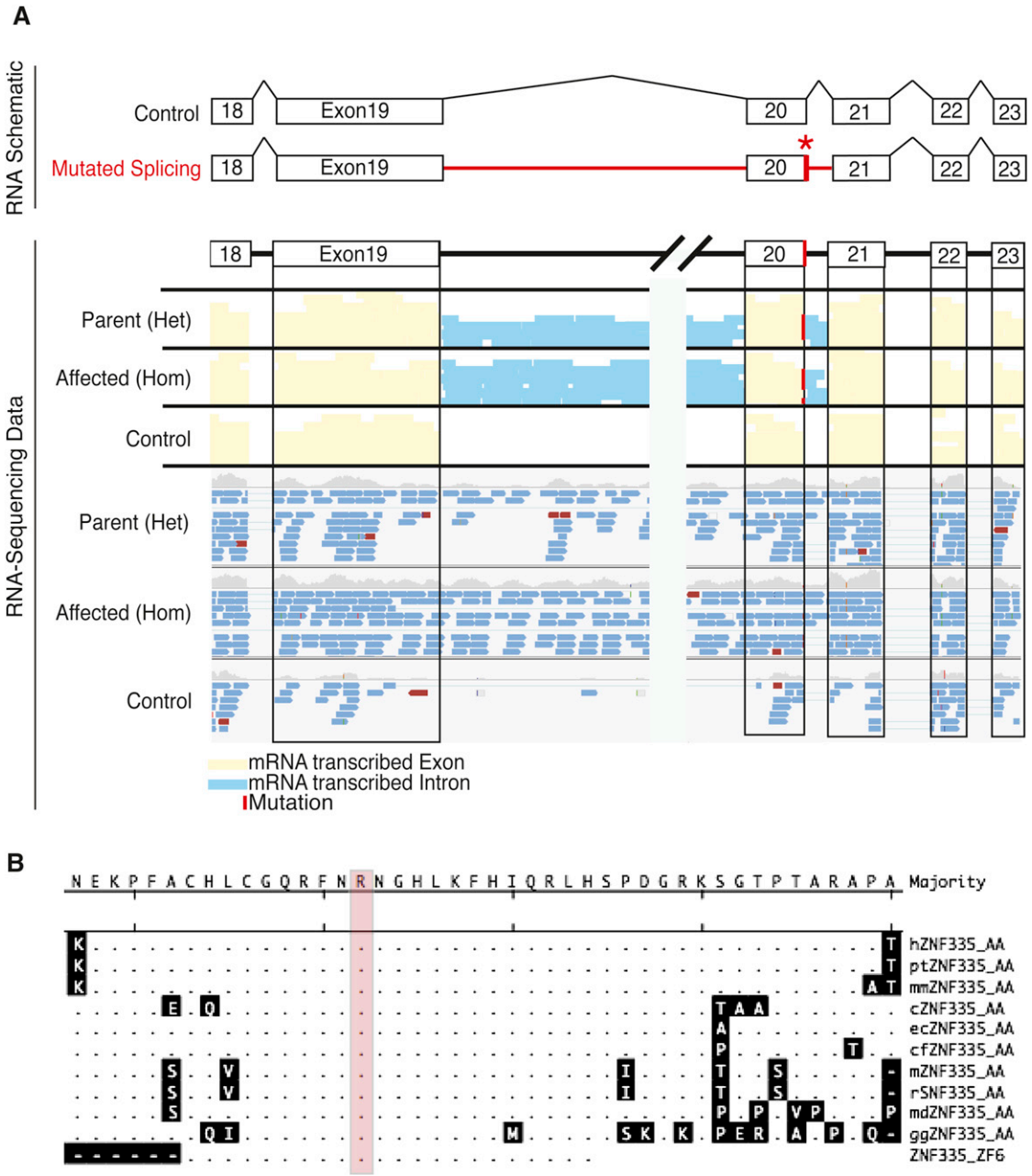

Figure S1. *ZNF335* RNA-Seq Data and ZNF335 Amino Acid Conservation, Related to Figure 2

(A) RNA-seq schematic of the data along with the raw reads picked up by RNA-seq showing the presence of the intron both before and after exon 20 containing the mutation (red). With an unbiased genome-wide search across all 354,244 Refseq-annotated introns for differentially transcribed introns in our patients compared to 7 control cell lines, the retained long intron of *ZNF335* is ranked as the 4th most significant differentially transcribed intron with an adjusted p-value of 1.57*E-31. The other top entries are not really included introns, but rather true differentially expressed genes in the patients, but in which there is an intron annotation that overlaps an alternative isoform's exon, thus making it a false positive.

(B) Analysis of the amino acid conservation of the arginine R 1111 in ZNF335 across a variety of different species. Top to bottom: human, chimp, macaque, cow, horse, dog, mouse, rat, opossum, chicken, zebrafish. ZNF335 is highly divergent in zebrafish and not detectable outside of vertebrates.

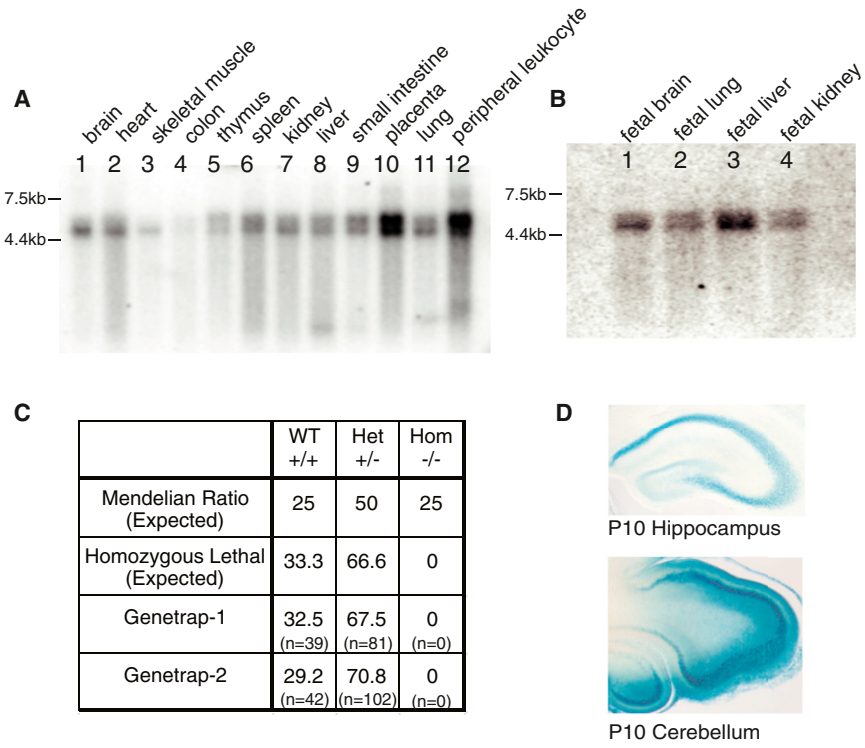

	WT +/+	Het +/-	Hom -/-
Mendelian Ratio (Expected)	25	50	25
Homozygous Lethal (Expected)	33.3	66.6	0
Genetrap-1	32.5 (n=39)	67.5 (n=81)	0 (n=0)
Genetrap-2	29.2 (n=42)	70.8 (n=102)	0 (n=0)

Figure S2. ZNF335 Is Expressed in a Variety of Tissues and Is Essential for Mouse Development, Related to Figure 3

(A and B) Northern blot analysis of *ZNF335* expression in a variety of adult (A) and embryonic (B) human organs show that *ZNF335* is ubiquitously expressed.

(C) Genotype segregation, as confirmed by PCR, of litters from $Znf335^{Genetrap/+}$ and $Znf335^{Genetrap/+}$ crosses show a complete absence of homozygous *genetrap* mice in both strains as early as E7.5 showing that *Znf335* is essential for mouse development and possibly implantation. n represents number of individual pups analyzed and found to contain that specific genotype.

(D) LacZ staining of developing hippocampus and developing cerebellum from a P10 $Znf335^{Genetrap/+}$ shows that ZNF335 is expressed in the P10 hippocampus and cerebellum.

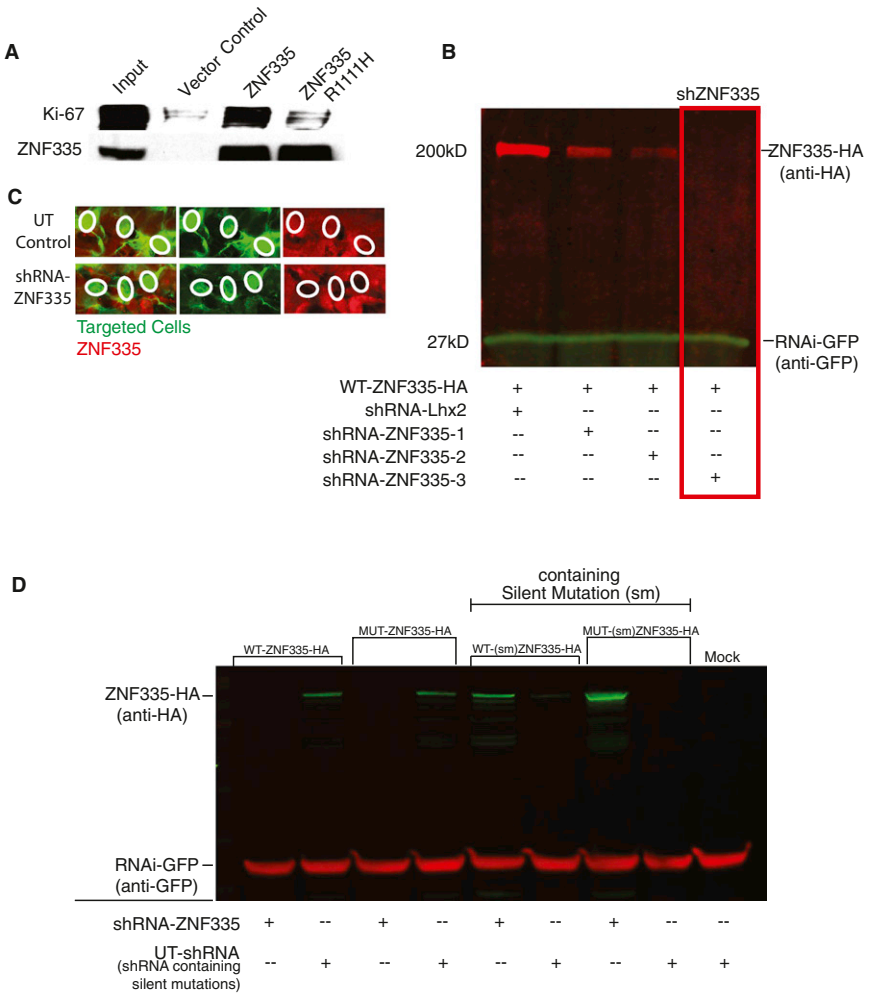

Figure S3. Knockdown Efficiency of shRNAs Targeted against *Znf335* and Characterization of Knockdown-Resistant Rescue Constructs, Related to Figure 4

(A) ZNF335 interacts with Ki67, a marker of proliferation. The mutation p.R1111H leads to a decrease of ZNF335 interaction with Ki67. The antibody is MIB1, which is a mouse monoclonal. It identifies two forms ~350kDa and 395 kDa in Western blotting. Ki-67 is a highly phosphorylated protein and as a result in some cells is detected in Western blotting as a broad band.

(B) Three different knockdown constructs were designed and shRNA-ZNF335-3 was utilized for all experiments, which knocks down up to 95% of protein after 24 hr.

(C) IHC analysis of cells 48 hr postelectroporation with shRNA-ZNF335 shows the lack of ZNF335 protein expression in comparison to control.

(D) The rescue expression constructs containing the silent mutation (sm) prevent the rescue constructs from being targeted by the shRNA-ZNF335. Co-transfections of shRNA-ZNF335 along with the rescue constructs (sm) allows for knockdown of endogenous ZNF335 and expression of the (sm) rescue construct at the same time. UT-shRNA (shRNA containing silent mutations) is the UT-Control construct utilized for all experiments.

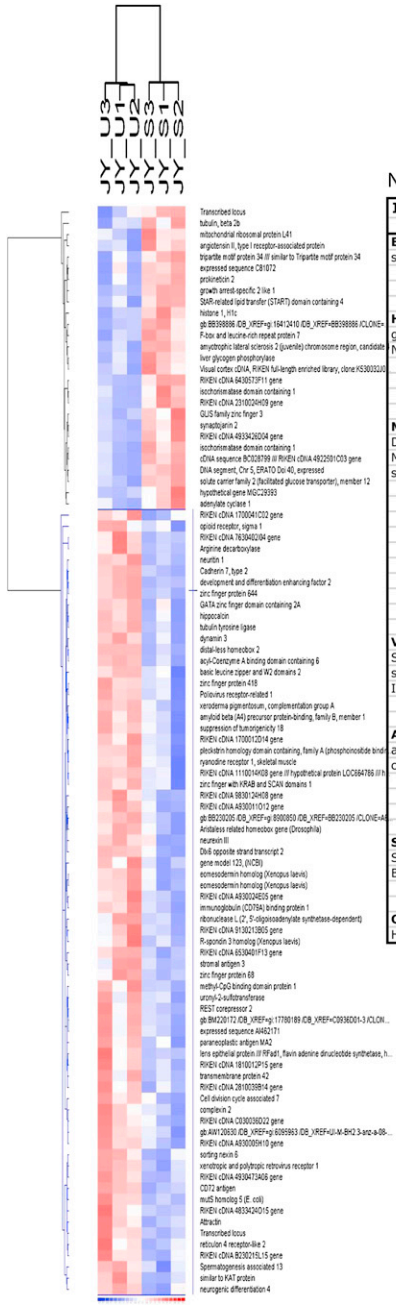

Notable Gene Chages

INCREASE	DECREASE
Brain Development	**Brain Development**
snail homolog-early TF (neural tube)	distal-less homeobox 2 (DLX2)-forebrain development
	DLX4-Craniofacial development
	DLX6
Hormone Signaling	**Neuron Development**
growth hormone receptor	neurogenin-TF for neurons
NREF2-thyroid hormone	Nuclear factor I/B-Transcription factor
	olig transcription factor 1
	Math1-granule neurons
	REST corepressor 2-neuronal differentiation
Microtubule/Actin	**Dendrites**
Dynein light chain	Neuritin-Neurite arborization/activity
MAP7	Tubulin tyrosin ligase-neurite outgrowth
synaptopodin 2-bnds actin in dendrites	Disabled homolog 1-Regulate Reelin (neurogenesis, dendrites)
	Cell Adhesion
	NCAM1-Cell adhesion
	Cadherin-Call adhesion
	Neurexin III-receptor adhesion
	Gene Regulation
	WDR61-transcription regulation through SKI/PAF (Histone)
	MeCP1-binds methylated DNA
Vesicle	**Vesicle**
Synaptojanin-vesicle traffic	synaptic nuclear envelope
syntaxin binding protein 3A-SNARE	Complexin 2-regulate SNARE/VAMP
Intersectin 2-Clatherin Endocytosis	dynamin-clatherin coated cell membrane
	DDEF2-golgi plasma in brain
Activity	**Activity**
annexin A11-calcium binding protein	Hippocalcin-Neuronal calcium sensor
chloride intracellular channel 5	Sodium channel, Type IV, beta-voltage gated
	Cell Cycle
	CDC7
Signaling	**Signaling**
SKI like-inhibit TGFB	IGFBP1
BMP5-TGFB family	Secreted frizzled related protein 1-Wnt signaling
	sorting nexin 6-TGFB family
OTHER	**OTHER**
Histone H1C	Amyloid beta (APP)

Figure S4. Microarray Analysis of Changes in Gene Expression upon Long-Term Knockdown of ZNF335, Related to Figure 5

Cells electroporated with shRNA-ZNF335 versus UT-Control at E14.5 were allowed to mature until embryos were P0 and the dissociated. GFP-positive (targeted cells) were selected for using FACS analysis and RNA from the two cell populations were utilized for microarray analysis. Knockdown of ZNF335 for four days led to changes in expression of genes important for neuronal differentiation and activity. S1-S3 (shRNA-ZNF335 knockdown cells), U1-U3 (UT-control cells) as summarized in the tables next to the heat map of changes in gene expression. Red = increase in expression, Blue = decrease in expression. Genes presented show a greater than 1.5 fold change with a P value of equal or less than 0.05. Microarray data is available online. Please see Supplemental Materials & Methods.

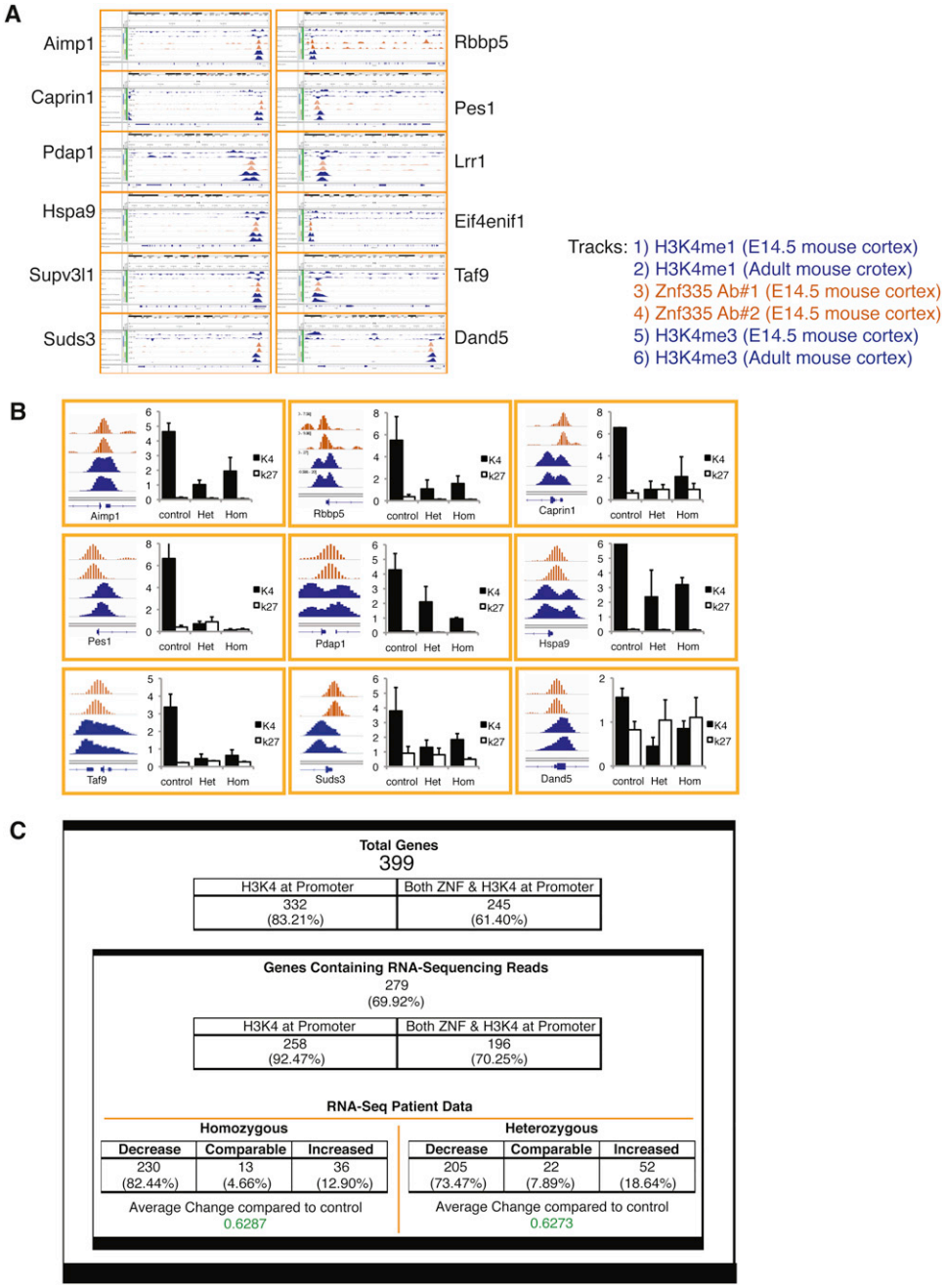

Figure S5. ChIP-Seq Binding of ZNF335 and Changes in Histone Modifications in the Absence of ZNF335, Related to Figure 6

(A) ZNF335 binds to promoter regions of a variety of different genes, and this binding overlaps with the H3K4me3 binding sites but not the H3K4me1 binding sites. ChIP-Sequencing peaks show that the ZNF335 complex binds to promoter regions of several genes important in brain development such as *Aimp1*, *Caprin1*, *Pdap1*, *Hspa9*, *Supv3l1*, *Suds3*, *Rbbp5*, *Pes1*, *Lrr1*, *Eif4enif1*, *Taf9*, *Dand5*. Top two tracks (blue) show H3K4me1 peaks at these promoters (Shen et al., 2012), Middle two tracks (orange) per gene is from ChIP-Seq data with two different antisera raised against ZNF335. Bottom two tracks (blue) show H3K4me3 peaks at these promoters (Shen et al., 2012). The ZNF335-bound peaks overlap with H3K4me3 peaks of these promoters, but not with the H3K4me1 peaks. See also Table S2.

(B) Close up analysis of the overlap of the peaks for ZNF335 binding (orange) and H3K4me3 (blue) peaks at the promoter region of representative genes. ChIP-qPCR Analysis of changes in H3K4me3 levels (black bars) versus the control H3K27me3 levels (white bars) show that there is a decrease in the levels of H3k4me3 levels in the heterozygous parents and homozygous patients while there is no change in H3K27me3. (AIMP1: K4: Control: 4.63 ± 0.58, Het Parent: 1.02 ± 0.3, Hom Patient: 1.94 ± 0.93; K27: Control: 0.12 ± 0.05, Het Parent: 0.08 ± 0.04, Hom Patient: 0.05 ± 0.03. Rbbp5: K4: Control: 5.5 ± 2.15, Het Parent: 1.08 ± 0.81, Hom Patient: 1.57 ± 0.69; K27: Control: 0.37 ± 0.2, Het Parent: 0.12 ± 0.05, Hom Patient: 0.12 ± 0.03.Caprin1: K4: Control: 6.56 ± 0.01, Het Parent: 0.95 ± 0.75, Hom Patient: 2.11 ± 1.8; K27: Control: 0.62 ± 0.23, Het Parent: 0.95 ± 0.43, Hom Patient: 0.95 ± 0.54. Pes1: K4: Control: 6.63 ± 2.54, Het Parent: 0.7 ± 0.23,

Hom Patient: 0.14 ± 0.11; K27: Control: 0.41 ± 0.16, Het Parent: 0.89 ± 0.45, Hom Patient: 0.19 ± 0.09. Pdap1: K4: Control: 4.28 ± 1.11, Het Parent: 2.1 ± 1.05, Hom Patient: 0.96 ± 0.08; K27: Control: 0.11 ± 0.02, Het Parent: 0.03 ± 0.02, Hom Patient: 0.05 ± 0.02. Hspa9: K4: Control: 6.2 ± 0.78, Het Parent: 2.36 ± 1.8, Hom Patient: 3.2 ± 0.5; K27: Control: 0.14 ± 0.04, Het Parent: 0.12 ± 0.02, Hom Patient: 0.1 ± 0.05. Taf9: K4: Control: 3.38 ± 0.73, Het Parent: 0.45 ± 0.26, Hom Patient: 0.63 ± 0.32; K27: Control: 0.23 ± 0.01, Het Parent: 0.32 ± 0.02, Hom Patient: 0.27 ± 0.03. Suds3: K4: Control: 3.79 ± 1.6, Het Parent: 1.31 ± 0.49, Hom Patient: 1.84 ± 0.41; K27: Control: 0.91 ± 0.46, Het Parent: 0.81 ± 0.45, Hom Patient: 0.50 ± 0.09. Dand5: K4: Control: 1.56 ± 0.2, Het Parent: 0.45 ± 0.2, Hom Patient: 0.85 ± 0.18; K27: Control: 0.83 ± 0.19, Het Parent: 1.04 ± 0.46, Hom Patient: 1.1 ± 0.45. All numbers were compared to *GAPDH* control and normalized to input. IP DNA was pooled from two separate IPs from pooled chromatin from 3 cell lines. qPCR analysis was done using triplicates.

(C) ChIP-seq data analysis with H3K4me3 binding and gene expression levels. A total of 399 genes were picked up by both ChIP-seq using two distinct ZNF335 antisera. 83.21% of the genes had a peak at the H3K4 promoter while 61.40% had a peak that overlapped for ZNF335 and H3K4me3. Of all the genes detected, 69.92% of genes also had data for transcript expression levels in the heterozygous parents and homozygous patients as compared to the controls. The group of genes that were bound to by ZNF335 collectively showed a 0.6287 fold in expression in the homozygous patients and 0.6273 in the heterozygous parents as compared to the controls. As a whole, this pool of genes which are putative ZNF335 targets are significantly decreased in expression as compared to the global average of changes in all gene expression which normalized out to only 1.04, indicating roughly no change.

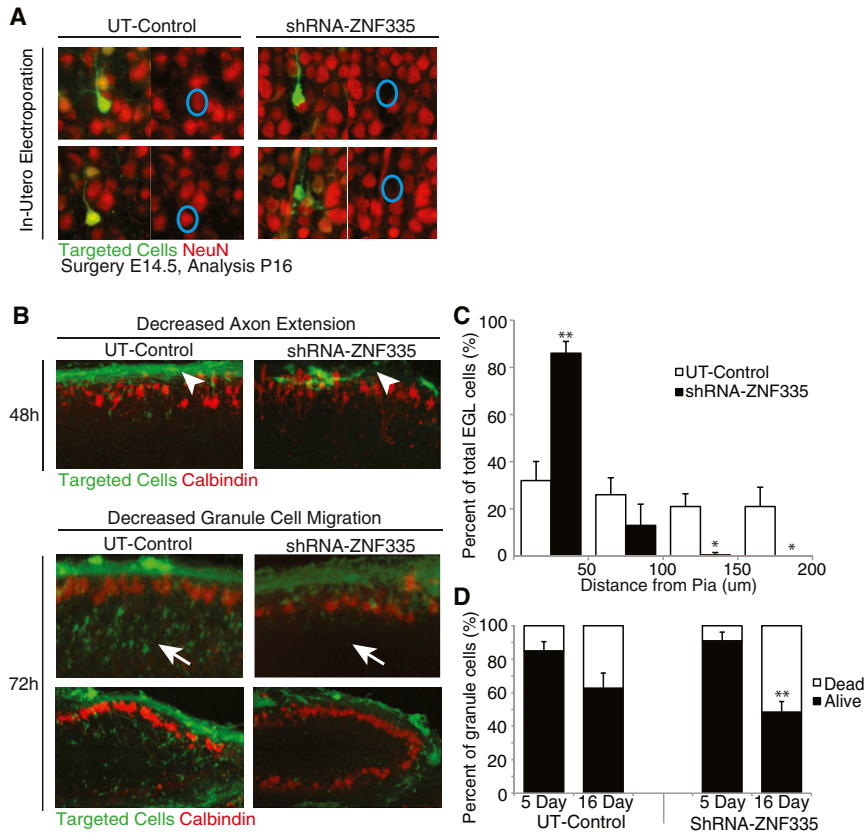

Figure S6. Incomplete Neuronal Differentiation and Granule Cell Migration upon Znf335 Knockdown, Related to Figure 7

(A) Similar to cortical cultures (Figure 7A, 7B), knockdown of ZNF335 in vivo through in utero electroporations also causes a lack of NeuN expression hinting at a state of incomplete neuronal differentiation.

(B) To assess the affects of knockdown of ZNF335 on migration, we selectively removed *ZNF335* from granule cell progenitors using shRNA-ZNF335 and UT-Control, and then prepared cerebellar slice cultures. At 48hr post electroporation, developing knockdown granule cells exhibited delayed axon extension, sending out shortened filopodia-like extensions, although these axons extended by 72hr. There are abnormal axonal extension (upper panel, arrowhead) and delayed migration of granule neurons (lower panels, arrows) past the Purkinje cell layer (Calbindin-stained) upon knockdown of ZNF335 at 48hours and 72hours post electroporation, respectively.

(C) By 72hrs post knockdown, granule cells that would normally have migrated past the Purkinje cell layer into the IGL were retarded in their migration. Not only did fewer cells migrate, they also migrated a shorter distance past the Purkinje cells. Since proper migration and interaction with Purkinje cells strongly influence the survival of granule cells (Morrison and Mason, 1998; Smeyne et al., 1995), the roles of ZNF335 in regulating proliferation, migration, and differentiation of granule cells provide a likely cause for the cell sparse granule cell layer (GCL) seen in the patients (Figure 1D). Granule cells, in turn, also regulate Purkinje cell orientation (Adams et al., 2002; Morrison and Mason, 1998; Nagata et al., 2006), thus the decreased number of granule cells present in the patients, and also seen in our explant experiments, could be one of the reasons for the poorly oriented Purkinje cells present in the patients (Figure 1D). Distance of granule cell migration past the purkinje cell layer: (UT-Control: 50um: 33.5 ± 5.6; 100um: 26.2 ± 8.3; 150um: 22.8 ± 4.1; 200um: 23.1 ± 8.1; shRNA-ZNF335: 50um: 84.2 ± 7.3; 100um: 18.5 ± 4.3; 150um: 2.4 ± 1.8; 200um: 0.8 ± 0.4); Mean ±SD, t test, p values: 50um = 0.0007; 100um:0.2268; 150um:0.0014; 200um:0.0089; n = 3 separate experiments using 3 pups each.

(D) Granule Cell Survival Assay (UT-Control Alive: 5 day:85.0 ± 5.5; 16 day:64.0 ± 9.2; shRNA-ZNF335: 5 day:91.0 ± 5.2; 16 day: 47.1+/−6.1). Mean ±SD, t test, Pvalues: 5 dayP = 0.0302; 16 dayP = 0.0008; n = 9 separate experiments using 3 pups each.

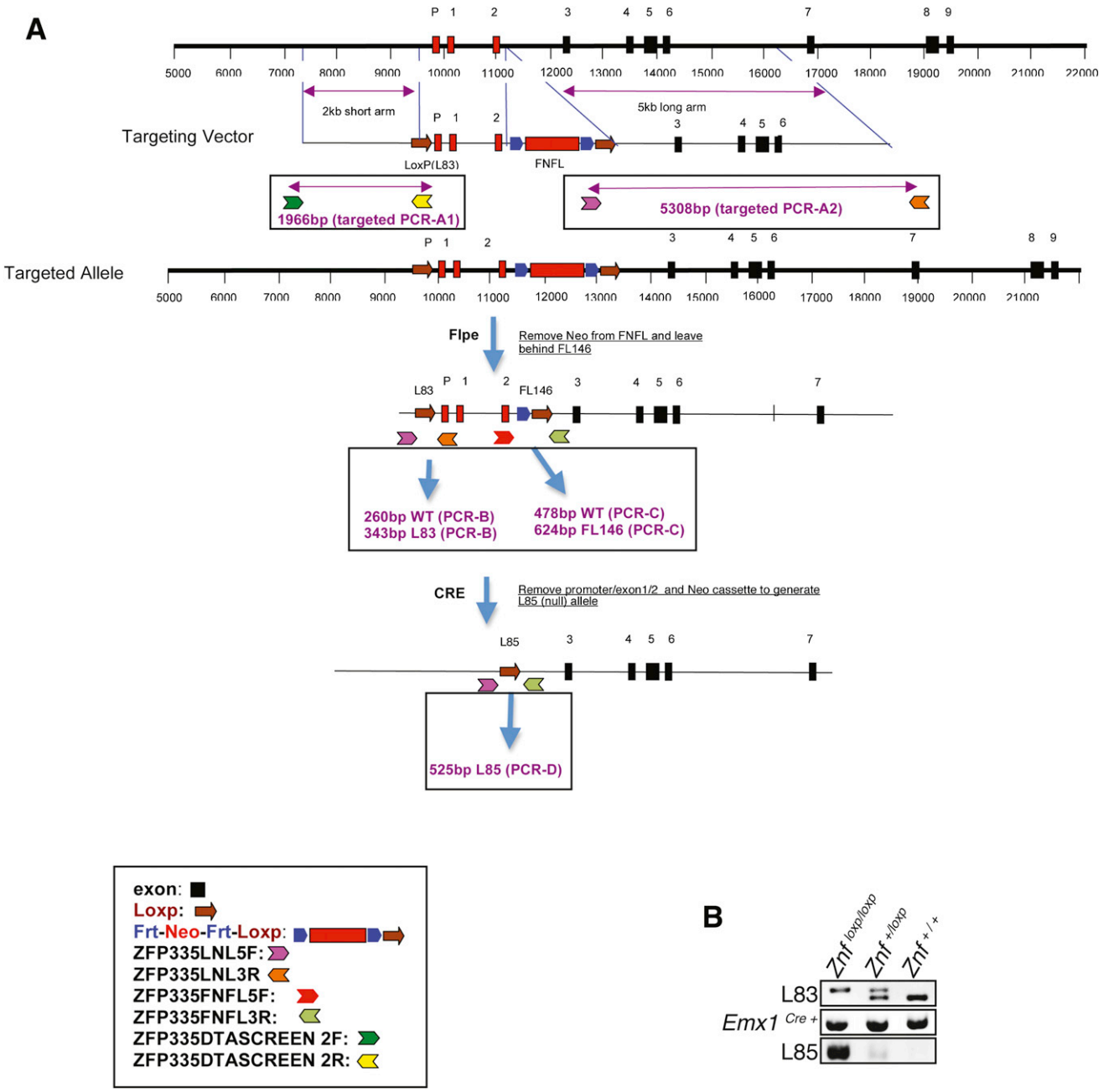

Figure S7. ZNF335 Conditional Knockout, Related to Figure 7

(A) The creation of the *Znf335-floxed* allele containing two loxp sites flanking the Promoter, Exon1, and Exon2 of *Znf335* essentially bypassing the initiation of *Znf335* transcript expression. No other putative promoters were found through the genome browser or while looking at H3K4me3 peaks or PolII peaks as a marker of gene promoter. See Supplemental Materials & Methods.

(B) Analysis and verification of the $Znf^{loxp/loxp}$:$Emx1^{Cre+}$, $Znf^{+/loxp}$:$Emx1^{Cre+}$, and $Znf^{+/+}$:$Emx1^{Cre+}$ mouse genotype. L83 products were from tail genomic DNA and L85 products were from DNA of developing forebrain tissue, where *Cre* is expressed.